Computational Mechanics
https://doi.org/10.1007/s00466-024-02522-z

ORIGINAL PAPER

Microplasticity in polycrystalline materials from thermal cycling

Anderson Nascimento[1] · **Akhilesh Pedgaonkar**[2] · **Curt A. Bronkhorst**[2] · **Irene J. Beyerlein**[1,3]

Received: 18 March 2024 / Accepted: 25 June 2024

Abstract

In this work, we present a finite deformation, fully coupled thermomechanical crystal plasticity framework. The model includes temperature dependence in the kinematic formulation, constitutive law and governing equilibrium equations. For demonstration, we employ the model to study the evolution and formation of residual stresses, residual statistically stored dislocation density and residual lattice rotation due solely to solid state thermal cycling. The calculations reveal the development of microplasticity within the microstructure provided that the temperature change in the thermal cycle is sufficiently large. They also show, for the first time, that the thermal cycling generates an internally evolving strain rate, where the contributions of mechanical strain and plasticity depend on temperature change. The calculations suggest a strong connection between the maximum temperature of a given cycle and the magnitude of the residual stresses generated after the cycle. A pronounced influence of elastic anisotropy on the heterogeneity of the residual stress distribution is also demonstrated here. Finally, we calculate lattice rotation obtained from thermal cycling ranging from ±0.4° and show the relation between changes in predominant slip systems with short range intragranular lattice rotation gradients. The model can benefit metal process design, especially where large strains and/or large temperature changes are involved, such as bulk forming and additive manufacturing.

Keywords Crystal plasticity · Thermomechanical modeling · Residual stress · Residual dislocation density · Residual lattice rotation

1 Introduction

Multiphysics modeling has become a key component of integrated computational materials engineering (ICME) [41, 90] and increasingly important to obtain in-depth understanding of a variety of relevant mechanisms and processes [20, 64]. Coupled thermomechanical models that account for the strong interplay between mechanical and thermal solution variables are a particular type of multiphysics framework. Their applications to mesoscale computational modeling are wide due to the pronounced impact of thermomechanical history on the constitutive response of polycrystalline materials [71]. In this context, Crystal plasticity (CP)-based modeling has matured into an established approach for describing the anisotropic deformation behavior of single crystalline and polycrystalline materials [73].

In recent times, understanding the thermomechanical behavior of materials has become crucial for elucidating the influence of various fabrication and processing techniques on mechanical properties. This interest spans across methods such as additive manufacturing (AM) [10, 29, 30] and bulk metal forming [26, 37, 82]. Residual stresses, whether arising from solid state thermal cycle (SSTC)—that is, heating and cooling steps with significant thermal variation due to the deposition of multiple layers of material—or from thermal gradients during cooling in hot bulk forming processes, play a pivotal role in determining the functionality and mechanical performance of the resulting parts [48]. In this context, thermomechanical CP models stand out as a compelling avenue for the quantification and assessment of these thermally induced residual stresses.

Thermomechanical coupling in CP-based models can be achieved in different ways. Owing to the considerable geometric implications of thermal expansion, the kinematic description is central to the coupling strategy [40]. Early works, such as those by McHugh et al. [58] and Srikanth and Zabaras [77] laid the foundation by incorporating thermal

---

✉ Anderson Nascimento
andersonw@ucsb.edu

[1] Department of Mechanical Engineering, University of California, Santa Barbara, CA 93106-5070, USA

[2] Department of Mechanical Engineering, University of Wisconsin, Madison, Wisconsin 53706, USA

[3] Materials Department, University of California, Santa Barbara, CA 93106-5050, USA

expansion into the deformation gradient to assess residual strains and thermal deformations, respectively. Meissonnier et al. [62] extended this approach utilizing an anisothermal deformation gradient to estimate stresses due to thermal expansion mismatch between different phases. Clayton [14] leveraged the kinematic thermal expansion in a comprehensive modeling framework to capture thermal expansion, softening and heat conduction in polycrystals under dynamic strain rates. Diani et al. [19] adopted an analogous kinematic formulation to obtain the stress-temperature response of shape memory polymers under constrained thermal expansion. Meier et al. [61] used the kinematic thermal expansion framework to assess thermally induced stresses due to temperature changes caused by current flow in aluminum conductors. Ozturk et al. [68] employed kinematic expansion to estimate the stresses due to anisothermal expansion of Ti alloys. Li et al. [49] adopted a fully-coupled framework to determine the response of BCC Ta at different strain rates and initial temperatures. Pokharel et al. [70] exploited a similar kinematic model to evaluate the residual stresses due to thermal processing in dual-phase microstructures of AMed 304 L stainless steel.

Thermomechanical coupling can also be introduced in order to model specific mechanisms. Luscher et al. [55] presented a thermomechanical framework featuring finite deformation kinematic decomposition and incorporating the temperature changes due to isentropic thermoelastic coupling, shock load heating and inelastic heating. Lieou et al. [51] outlined a thermodynamical treatment through state variable inclusion of grain boundary density to model thermal behavior with adiabatic shear banding and dynamic recrystallization in 316 L stainless steel. Connolly et al. [16] employed a thermomechanical framework, featuring kinematic expansion, to capture the effects of texture, phase morphology and temperature on the thermomechanical response of QP1180 steel. Bennett et al. [6] presented a thermoelastoplastic self-consistent formulation, with additive small strain decomposition to study thermal ratcheting of composites. Lieou and Bronkhorst [50] derived a relationship between the Taylor–Quinney coefficient, describing the fraction of plastic work converted into heat, and the effective temperature, demonstrating its validity through finite-element analysis on aluminum alloy 6016-T4.

While the kinematic expansion is central to the thermomechanical framework and mechanism targeted formulations are particularly useful, fully-coupled models still need to account for thermal dependence in the single crystal constitutive model. Due to the thermally-activated glide, the description of the evolution of dislocation structures is one of the ways in which the temperature sensitivity can be introduced into the constitutive response. In this context, Essmann and Mughrabi [23] described the mechanisms for dislocation annihilation and pointed out the importance of temperature for the annihilation of screw dislocations by cross-slip. Later, Mecking and Kocks [60] modeled the evolution of the flow stress as a function of the current dislocation density as well as the rate of change of the dislocation density. The latter was described by a dislocation storage component, geometric in nature, and a dislocation annihilation component, strongly dependent on thermal activation. Such framework established the foundation for the next generation of constitutive models. Arsenlis and Parks [3] modeled the evolution of dislocation density through internal functions describing the average thermally activated dislocation mobility, average segment length and annihilation distance. Ma and Roters [56] presented a formulation suitable for FCC Al at elevated temperatures, distinguishing between dislocation cell blocks and dense dislocation cell walls. Beyerlein and Tomé[8] developed a constitutive formulation for HCP Zr including specific hardening laws for different slip and twinning modes, each with their respective temperature dependence. The first through thermally-activated recovery and the second through the slip-twin interaction. Shanthraj and Zikry [75] formulated a set of evolution equations explicitly accounting for the glissile and sessile dislocation populations and described the annihilation rate through an Arrhenius-type equation. More recently, Upadhyay [83] developed a small-strain framework suitable for studying dislocation structure evolution in heat-affected zones. Hunter and Preston [45] developed dislocation density evolution equations including explicit equations for both sessile and glissile densities accounting for a variety of formation and annihilation mechanisms under a wide range of temperatures. Hu et al. [44] integrated continuum dislocation dynamics and CP to simulate the formation and stability of dislocation structures under thermal conditions seen in AM. Lima-Chaves and Upadhyay [52] implemented a small-strain FE scheme to directly assess the influence of dislocation glide on temperature evolution.

Temperature effects on dislocation glide are sensitive to intragranular microstructure, particularly in cases where the grains contain a network of fine precipitates, such as in Ni-based superalloys. Several sophisticated single crystal hardening laws have been implemented into the constitutive response to account for dislocation interactions with the γ' and γ'' precipitates. As an example, Ghorbanpour et al. [33] built a model for the Ni-based superalloy IN718 considering solid solution effects, precipitate shearing, grain size, grain shape, non-Schmid effects, backstress and dislocation density evolution under different loading orientations and reverse loading. Ghorbanpour et al. [31] later used this model to study the response of this same material as a function of temperature. Agaram et al. [1] developed a CP model to incorporate through a probabilistic representation, the effects of precipitates on IN718 under monotonic and cyclic loading. Chan [11] incorporated of dislocation pileups and its breakdown into cross slip into a phenomenological Ramberg-Osgood model to capture the response of Ni-based superalloys under monotonic and cyclic loading.

In addition to thermal dependence in the kinematic description and constitutive model, the coupling between the mechanical and thermal field equations is a key component of the thermomechanical framework. This coupling is pivotal across a spectrum of processes, where thermal gradients—whether from layer-by-layer deposition, welding, or bulk metal forming—play a significant role in influencing the material's mechanical behavior. Denlinger et al. [18] used a coupled framework to predict distortion in large-scale Ti-6Al-4V AMed parts through thermoelastoplastic analysis and adaptive coarsening. Ren et al. [72] presented a thermomechanical model to assess the effects of dynamic temperature evolution and laser deposition strategies on residual stress and distortion in SS316L. Singh et al. [76] studied the effect of layer thickness on residual stress evolution in laser power bed fusion (LPBF) of of IN718 with FE thermomechanical simulations obtaining high residual stresses due to thermal gradient. Weisz-Patrault et al. [87] combined in-situ monitoring and decoupled thermomechanical modeling to analyze manufacturing strains and residual stresses in AMed thin-walled structures.

While the studies described present various methods for achieving thermomechanical coupling, most focus on one or two of the three key areas—kinematic description, constitutive modeling, or governing equations—without fully integrating the thermal aspects across all three. This approach results in a partial coupling that may not fully encapsulate the intricacies of thermomechanical behavior.

In this work, we present a large strain, fully coupled thermomechanical CP framework. Thermal dependence is incorporated in the kinematics, constitutive model, and governing equations for adequate assessment of the thermomechanical response. As a model material, we elect to apply the computational framework to Inconel 718 (IN718), a nickel-based superalloy. Towards this goal, the IN718 constitutive response includes deformation via anisotropic elasticity and crystallographic slip for an FCC crystal [12, 38, 39]. Our immediate interest here lies in understanding the results on the micromechanical fields as a function of thermal cycling only. Many of the important microscopic microstructure features and their effect on individual dislocations that are not taken into account into the present hardening law can be incorporated in a straightforward manner.

For demonstration, the framework is employed to study the evolution and formation of residual stresses, statistically stored dislocation (SSD) density, and lattice rotation originating from thermal cycling, starting from room temperature, rising to a peak value, and returning to room temperature. This approach allows us to analyze the macroscopic average response and subgrain spatial fields, including localized residual stresses, heterogeneity of residual SSD density, and intragranular lattice rotation gradients. The calculations reveal a strong connection between thermal amplitude, characterized by the maximum temperature achieved above room temperature, and the magnitude of residual stresses. They also highlight microplasticity, evidenced by residual stresses and a positive dislocation storage rate, even for macroscopic thermoelastic cycling. Moreover, the microstructure experiences an evolving strain rate during thermal cycling, which alone can induce the evolution of SSD density, particularly at grain boundaries and triple junctions. Finally, we calculate the intragranular lattice rotations obtained from thermal cycles at different thermal amplitudes and associate intragranular lattice rotation gradients with local changes in predominant slip systems.

This paper is structured as follows. First, the kinematics accounting for elastic, plastic, and thermal elastic expansion is presented in Sect. 2. We then describe the single crystal constitutive model in Sect. 3, after which the discretization and numerical integration of the CP framework is delineated in Sect. 4. The governing equations for the thermomechanical BVP are summarized in Sect. 5. The methodology closes with Sect. 6 describing the computational setup, boundary conditions and material parameters. Next, the results are presented in Sect. 7, where the residual stresses, strain rate evolution, stored dislocation density and lattice rotation during and after thermal cycling are evaluated. We then discuss the impact of the results in light of previous studies in Sect. 8. The paper concludes with Sect. 9, a summary of the main modeling contribution and findings.

2 Kinematics

We initially consider a one-to-one mapping $\boldsymbol{\varphi}$ of the body $\mathcal{B}$ from reference to current configuration, defined over every material point $\boldsymbol{X}$ by:

$$\boldsymbol{\varphi}(\boldsymbol{X}) : \mathcal{B}_0 \rightarrow \mathcal{B}_{\mathrm{t}}. \tag{1}$$

The corresponding deformation gradient is written as:

$$\boldsymbol{F} = \frac{\partial \boldsymbol{\varphi}}{\partial \boldsymbol{X}}. \tag{2}$$

The conventional multiplicative decomposition of $\boldsymbol{F}$ into elastic and plastic components is extended to include anisothermal effects and takes the form [62, 77]:

$$\boldsymbol{F} = \boldsymbol{F}^{\mathrm{e}} \boldsymbol{F}^{\mathrm{p}} \boldsymbol{F}^{\theta}. \tag{3}$$

The decomposition presented in Eq. (3) computes the inelastic response after the application of thermal expansion/contraction to the lattice. This effectively allows us to include thermal expansion effects on plastic deformation. It contrasts with the formulation presented by McHugh et al. [58] where $\boldsymbol{F} = \boldsymbol{F}^{\mathrm{e}} \boldsymbol{F}^{\theta} \boldsymbol{F}^{\mathrm{p}}$, i.e., the plastic response is calculated before considering lattice expansion/contraction. The thermal deformation gradient is defined as:

$$\boldsymbol{F}^{\theta} = \exp\left\{(\theta - \theta_0)\boldsymbol{\beta}\right\}, \tag{4}$$

where $\boldsymbol{\beta}$ denotes the diagonal thermal expansion tensor comprised of the coefficients of thermal expansion of the lattice and θ_0 the reference temperature, here taken as room temperature. The evolution of the thermal deformation gradient can be obtained from Eq. (4) and is given by:

$$\dot{\boldsymbol{F}}^{\theta} = \dot{\theta}\boldsymbol{\beta}\boldsymbol{F}^{\theta}. \tag{5}$$

Upon application of thermal loading, the plastic response can be assessed, and the evolution of the plastic deformation gradient is obtained by:

$$\dot{\boldsymbol{F}}^{\mathrm{p}} = \boldsymbol{L}^{\mathrm{p}} \boldsymbol{F}^{\mathrm{p}}, \quad \boldsymbol{L}^{\mathrm{p}} = \sum_{\alpha} \dot{\gamma}^{\alpha} \boldsymbol{S}_0^{\alpha}, \tag{6}$$

where $\boldsymbol{L}^{\mathrm{p}}$ is the plastic velocity gradient and $\dot{\gamma}^{\alpha}$ the slip rate on the slip system α. The SCHMID tensor in Eq. (6) is defined in the reference configuration by $\boldsymbol{S}_0^{\alpha} = \boldsymbol{m}_0^{\alpha} \otimes \boldsymbol{n}_0^{\alpha}$, where $\boldsymbol{m}_0^{\alpha}$ denotes the slip direction and $\boldsymbol{n}_0^{\alpha}$ the slip plane normal.

3 Constitutive law

The single crystal constitutive response in the intermediate configuration is assessed by means of the GREEN-LAGRANGE strain tensor and its stress work-conjugate, the second PIOLA- KIRCHHOFF stress tensor, which are respectively given by:

$$\boldsymbol{E}^{e} = \frac{1}{2}\left(\boldsymbol{F}^{\mathrm{e}\,\mathrm{T}} \boldsymbol{F}^{\mathrm{e}} - \boldsymbol{I}\right), \tag{7a}$$

$$\boldsymbol{S} = \mathbb{C} : \boldsymbol{E}^{e}, \tag{7b}$$

where $\mathbb{C}$ is the temperature dependent elastic stiffness tensor, which in crystal coordinates is defined as:

$$\mathbb{C}^{c}_{ijkl}(\theta) = \mathbb{C}_{ijkl} + \mathbb{M}_{ijkl}\theta, \tag{8}$$

with $\mathbb{C}_{ijkl}$ denoting the elastic stiffness tensor at room temperature and $\mathbb{M}_{ijkl}$ the rate of change of the elastic moduli with respect to θ. The mapping of $\mathbb{C}^{c}_{ijkl}(\theta)$ from crystal to global basis is done by means of the rotation matrix $\tilde{\boldsymbol{R}}$, precisely:

$$\mathbb{C}_{ijkl} = \tilde{R}_{im}\tilde{R}_{jn}\tilde{R}_{kp}\tilde{R}_{lq}\mathbb{C}^{c}_{mnpq}. \tag{9}$$

The CAUCHY stress tensor is obtained by pushing-forward the second PIOLA- KIRCHHOFF stress into the current configuration:

$$\boldsymbol{\sigma} = \frac{1}{\det \boldsymbol{F}^{\mathrm{e}}}\left(\boldsymbol{F}^{\mathrm{e}} \boldsymbol{S} \boldsymbol{F}^{\mathrm{e}\,\mathrm{T}}\right). \tag{10}$$

The resolved shear stress (RSS) on a particular slip system α is approximated by:

$$\tau^{\alpha} = \det \boldsymbol{F}^{\theta}\left(\boldsymbol{F}^{\theta\,\mathrm{T}} \boldsymbol{S} \boldsymbol{F}^{\theta\,-\mathrm{T}}\right) : \boldsymbol{S}_0^{\alpha}. \tag{11}$$

The plastic slip rate on each slip system is then computed by a rate-dependent power law [69]:

$$\dot{\gamma}^{\alpha} = \dot{\gamma}_0 \left|\frac{\tau^{\alpha}}{g^{\alpha}}\right|^{n} \operatorname{sgn}\left(\tau^{\alpha}\right), \tag{12}$$

where $\dot{\gamma}_0$ is the reference slip rate, n the power law exponent and g^{α} the slip resistance on slip system α. The slip resistance follows a Taylor-type formulation presented by Franciosi et al. [27] and is given by:

$$g^{\alpha} = g_0 + \kappa b \mu \sqrt{\sum_{\beta} a^{\alpha\beta}\rho^{\beta}}, \tag{13}$$

with g_0 as the constant initial slip resistance, κ the dislocation interaction coefficient, b the magnitude of the Burgers vector, ρ the dislocation density on a particular system and $a^{\alpha\beta}$ the dislocation interaction matrix accounting for both self and latent hardening. The temperature dependent effective shear modulus, μ, is obtained from the elastic parameters as [47]:

$$\mu(\theta) = \sqrt{C_{44}(\theta)\frac{C_{11}(\theta) - C_{12}(\theta)}{2}}. \tag{14}$$

The dislocation density evolution follows the Kocks-Mecking formulation [60] and is given by:

$$\dot{\rho}^{\alpha} = \frac{1}{b}\left(\frac{1}{K}\sqrt{\sum_{\beta} a^{\alpha\beta}\rho^{\beta}} - 2y_c^{\alpha}\rho^{\alpha}\right)|\dot{\gamma}^{\alpha}|. \tag{15}$$

The first term in Eq. (15) describes the rate of dislocation generation/storage with K denoting the mean free path coefficient. The second term describes the rate of dislocation removal with y_c^{α} representing the critical annihilation distance, which has its evolution modeled by:

$$y_c^{\alpha} = y_0\left(\frac{|\dot{\gamma}^{\alpha}|}{\dot{\gamma}_0}\right)^{(k_B\theta/A)}, \tag{16}$$

where y_0 is the reference annihilation distance, k_{B} the Boltzmann constant and A the recovery activation energy. From

Eqs. (13) and (15), the evolution of the slip resistance is obtained as:

$$\dot{g}^{\alpha} = \frac{\partial g^{\alpha}}{\partial \rho}\frac{\partial \rho}{\partial t} = \sum_{\beta} h^{\alpha\beta} |\dot{\gamma}^{\beta}|, \tag{17}$$

with $h^{\alpha\beta}$ related directly to dislocation interaction factors and dislocation density via:

$$h^{\alpha\beta} = \kappa\mu \left(\frac{\frac{1}{K}\sqrt{\sum_{\zeta} a^{\beta\zeta}\rho^{\zeta}} - 2y_c^{\beta}\rho^{\beta}}{2\sqrt{\sum_{\zeta} a^{\beta\zeta}\rho^{\zeta}}} \right) a^{\alpha\beta}. \tag{18}$$

The last component of the single crystal constitutive model accounts for the inelastic heat generation and is given by:

$$\dot{Q} = \eta \sum_{\alpha=1}^{n} \tau^{\alpha}\dot{\gamma}^{\alpha}, \tag{19}$$

where η represents the Taylor–Quinney coefficient [79] estimating the fraction of plastic work converted into heat.

4 Discretization and numerical integration

The discretization of the single crystal constitutive model outlined in Sect. 3 follows the procedure for implicit integration within a finite element (FE) framework [4, 17, 46]. It is further extended to include the thermal expansion kinematics outlined in Sect. 2 [62]. The notation $t_n = t$ and $t_{n+1} = t + \Delta t$ is used to represent the beginning and the end of an arbitrary time interval $[t_n, t_{n+1}]$. All quantities are evaluated at t_{n+1}, unless explicitly specified.

We initially obtain the incremental form of the thermal deformation gradient evolution and its inverse by integrating Eq. (5) over $[t_n, t_{n+1}]$ and using first order approximations for $\exp(\pm\Delta\theta\boldsymbol{\beta})$, precisely:

$$\boldsymbol{F}^{\theta} = \exp(\Delta\theta\boldsymbol{\beta})\,\boldsymbol{F}^{\theta}(t_n) \approx (\boldsymbol{I} + \Delta\theta\boldsymbol{\beta})\,\boldsymbol{F}^{\theta}(t_n), \tag{20a}$$

$$\boldsymbol{F}^{\theta^{-1}} = \boldsymbol{F}^{\theta^{-1}}(t_n)\exp(-\Delta\theta\boldsymbol{\beta}) \approx \boldsymbol{F}^{\theta^{-1}}(t_n)\,(\boldsymbol{I} - \Delta\theta\boldsymbol{\beta}), \tag{20b}$$

where $\Delta\theta = \dot{\theta}\Delta t$ denotes the temperature increment. Similarly, the incremental form of the plastic deformation gradient and its inverse are obtained from Eq. (6) as:

$$\boldsymbol{F}^{\mathrm{p}} \approx \left(\boldsymbol{I} - \sum_{\alpha} \Delta\gamma^{\alpha}\boldsymbol{S}_0^{\alpha}\right)^{-1} \boldsymbol{F}^{\mathrm{p}}(t_n), \tag{21a}$$

$$\boldsymbol{F}^{\mathrm{p}^{-1}} \approx \boldsymbol{F}^{\mathrm{p}^{-1}}(t_n)\left(\boldsymbol{I} - \sum_{\alpha} \Delta\gamma^{\alpha}\boldsymbol{S}_0^{\alpha}\right), \tag{21b}$$

with $\Delta\gamma^{\alpha} = \dot{\gamma}^{\alpha}\Delta t$ denoting the slip increment. The elastic deformation gradient can be expressed in terms of $\boldsymbol{F}$, $\boldsymbol{F}^{\theta^{-1}}(t_n)$ and $\boldsymbol{F}^{\mathrm{p}^{-1}}(t_n)$ as:

$$\begin{aligned}\boldsymbol{F}^{\mathrm{e}} = \boldsymbol{F}\boldsymbol{F}^{\theta^{-1}}\boldsymbol{F}^{\mathrm{p}^{-1}} &= \boldsymbol{F}\boldsymbol{F}^{\theta^{-1}}(t_n)\,(\boldsymbol{I} - \Delta\theta\boldsymbol{\beta})\\ &\boldsymbol{F}^{\mathrm{p}^{-1}}(t_n)\left(\boldsymbol{I} - \sum_{\alpha} \Delta\gamma^{\alpha}\boldsymbol{S}_0^{\alpha}\right).\end{aligned} \tag{22}$$

The GREEN- LAGRANGE strain tensor is then given by:

$$\boldsymbol{E}^{e} = \frac{1}{2}\left[\boldsymbol{A} - \boldsymbol{I} - \sum_{\alpha} \Delta\gamma^{\alpha}\left(\boldsymbol{S}_0^{\alpha^{\mathrm{T}}}\boldsymbol{A} + \boldsymbol{A}\boldsymbol{S}_0^{\alpha}\right)\right], \tag{23}$$

where $\boldsymbol{A}$ is written as:

$$\begin{aligned}\boldsymbol{A} = \boldsymbol{F}^{\mathrm{p}^{-\mathrm{T}}}(t_n)\,(\boldsymbol{I} - \Delta\theta\boldsymbol{\beta})&\\ \boldsymbol{F}^{\theta^{-\mathrm{T}}}(t_n)\boldsymbol{F}^{\mathrm{T}}\boldsymbol{F}\boldsymbol{F}^{\theta^{-1}}(t_n)\,(\boldsymbol{I} - \Delta\theta\boldsymbol{\beta})\,\boldsymbol{F}^{\mathrm{p}^{-1}}(t_n),&\end{aligned} \tag{24}$$

and we finally obtain the second PIOLA- KIRCHHOFF stress from Eq. (7b), precisely:

$$\begin{aligned}\boldsymbol{S} = \mathbb{C} : \boldsymbol{E}^{e} \approx \frac{1}{2}\mathbb{C} : (\boldsymbol{A} - \boldsymbol{I})&\\ - \sum_{\alpha} \Delta\gamma^{\alpha}\frac{1}{2}\mathbb{C} : \left(\boldsymbol{S}_0^{\alpha^{\mathrm{T}}}\boldsymbol{A} + \boldsymbol{A}\boldsymbol{S}_0^{\alpha}\right),&\end{aligned} \tag{25}$$

$$= \boldsymbol{S}^{\mathrm{tr}} - \sum_{\alpha} \Delta\gamma^{\alpha}\boldsymbol{C}^{\alpha}, \tag{26}$$

where $\boldsymbol{S}^{\mathrm{tr}}$ and $\boldsymbol{C}^{\alpha}$ are respectively defined as:

$$\boldsymbol{S}^{\mathrm{tr}} = \frac{1}{2}\mathbb{C} : (\boldsymbol{A} - \boldsymbol{I}), \tag{27a}$$

$$\boldsymbol{C}^{\alpha} = \frac{1}{2}\mathbb{C} : \left(\boldsymbol{S}_0^{\alpha^{\mathrm{T}}}\boldsymbol{A} + \boldsymbol{A}\boldsymbol{S}_0^{\alpha}\right). \tag{27b}$$

The implicit integration of Eq. (26) coupled with the evolution of the slip resistance follows the two-level iterative procedure outlined by Kalidindi et al. [46] and Anand [2].

5 Governing equations

The fully-coupled thermomechanical framework assumes a strong interplay between the mechanical and thermal solution variables [67]. This assumption entails the simultaneous solution of the governing equations expressing the balance of momentum and the balance of energy, which are summarized here.

The balance of momentum due to a motion acting on a body $\mathcal{B}$, alongside its initial and boundary conditions, is commonly expressed by:

$$\operatorname{div}\boldsymbol{\sigma} = \boldsymbol{0}, \tag{28a}$$

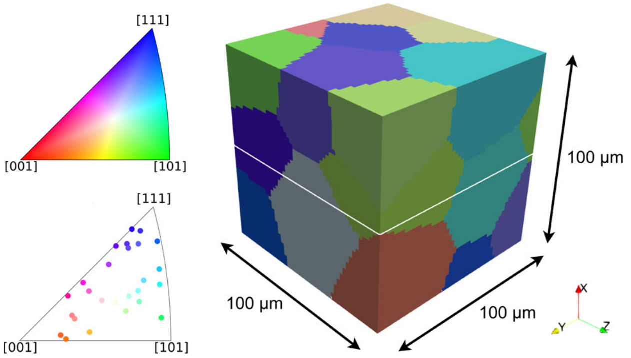

Fig. 1 Highly-resolved IN718 oligocrystal RVE with 26 grains randomly oriented used in the analysis. Cut C_x at mid-height is used for reference in the following sections

$$\boldsymbol{u}(\boldsymbol{X}, \mathbf{0}) = \boldsymbol{u}_0 \quad \text{at } \mathcal{B}, \tag{28b}$$

$$\boldsymbol{u}(\boldsymbol{X}, t) = \boldsymbol{u}^* \quad \text{at } \partial\mathcal{B}^u, \tag{28c}$$

$$\boldsymbol{\sigma} \cdot \boldsymbol{n} = \boldsymbol{t}^* \quad \text{at } \partial\mathcal{B}^\sigma, \tag{28d}$$

Equation (28a) is expressed in a simplified form considering the absence of inertial and body forces. Equation (28b) defines the initial condition to the mechanical problem by describing the displacement field at $t = 0$. Equations (28c) and (28d) represent the DIRICHLET and NEUMANN boundary conditions respectively.

The thermal field equation expresses the balance of energy on a body $\mathcal{B}$. It can be written, alongside its initial and boundary conditions as:

$$\bar{\rho}\bar{c}\dot{\theta} = \operatorname{div} \boldsymbol{q} + \dot{Q}, \tag{29a}$$

$$\theta(\boldsymbol{X}, \mathbf{0}) = \theta_0 \quad \text{at } \mathcal{B}, \tag{29b}$$

$$\theta(\boldsymbol{X}, t) = \theta^* \quad \text{at } \partial\mathcal{B}^\theta, \tag{29c}$$

$$\boldsymbol{q} \cdot \boldsymbol{n} = Q^* \quad \text{at } \partial\mathcal{B}^q, \tag{29d}$$

where $\bar{\rho}$, $\bar{c}$, $\boldsymbol{q}$ and $\dot{Q}$ are respectively the density, specific heat, heat flux and volumetric heat generation. Equation (29b) defines the initial condition to the thermal problem by describing the temperature field at $t = 0$. Equations (29c) and (29d) represent the DIRICHLET and NEUMANN boundary conditions respectively.

The mathematical framework outlined here, in conjunction with the thermal dependence introduced into the kinematic model and single crystal constitutive law, defines a fully coupled thermoelastoplastic boundary value problem (BVP).

6 Computational model

We demonstrate the applicability of the thermomechanical model presented in the previous sections by analyzing the partially constrained expansion of an IN718 oligocrystal under thermal load. IN718's mechanical response has been replicated successfully by a variety of CP based models, from polycrystalline plasticity models [31] to spatially resolve full field models such as crystal plasticity finite element (CPFE) [38, 39], and crystal plasticity fast FOURIER transform (CPFFT) [15], which assumed the predominant deformation mechanism was grain-scale slip. Its mechanical performance has also been studied both at room and high temperatures as well as in a wide range of strain-rates [25, 28, 31, 59]. IN718 can be AMed through different fabrication techniques such as selective laser melting (SLM), directed energy deposition (DED) as well as with hybrid approaches [34] and was originally designed for high-temperature applications [42]. It is, therefore, a suitable model material for this study owing to the considerable thermal gradients it experiences during the fabrication process, its applications across a broad spectrum of temperatures and in alignment with the recent efforts towards its modeling and characterization [32, 89].

Figure 1 illustrates the highly-resolved IN718 oligocrystal adopted in the analysis. The representative volume element (RVE) captures a microstructural volume of $100\,\mu\text{m}^3$ and features 26 grains randomly oriented. A total of 125000 elements are distributed in a $50 \times 50 \times 50$ voxelized mesh, providing a resolution of $2\,\mu\text{m}^3$ per element. We employ trilinear hexahedral elements of the C3D8T type from the Abaqus/Standard solid element library. These are suitable for fully coupled thermal-stress simulations in which both temperature and displacements are nodal degrees of freedom and the governing equations outlined in Sect. 5 are solved simultaneously.

The thermal boundary conditions imposed on the model are tailored to emulate elementary thermal cycles, which are characterized by a desired thermal amplitude at a given temperature rate. Heat flux in and out of the RVE is fully controlled by the prescribed flux at the top yz surface, defining a uni-dimensional temperature gradient along the x-axis. Heat flux is not considered in the remaining surfaces [86, 87]. The remaining surfaces are displacement-constrained in their normal directions. These thermomechanical boundary conditions, albeit simple, allow the assessment of the micromechanical response in view of the imposed thermal amplitudes and temperature rate.

The relevant constitutive parameters for IN718 are listed in Table 1. Values for the thermophysical parameters, namely, isotropic thermal expansion coefficient, density, specific heat and thermal conductivity were obtained from the literature [65]. The variability of the thermophysical parameters with respect to temperature is not considered here. Elastoplastic material parameters are obtained from the works of Martin et al. [57] and Hestroffer et al. [38], where they have been characterized using experimental data. The dependence of the

Table 1 Constitutive parameters used for IN718 [36, 38, 57, 65]

Property	Value	Unit	Property	Value	Unit
θ_0	298	K	n	20	–
β	13×10^{-6}	K^{-1}	g_0	400	MPa
$\bar{\rho}$	8190	$\mathrm{kg\,m^{-3}}$	κ	1	–
$\bar{c}$	435	$\mathrm{J\,kg^{-1}\,K^{-1}}$	b	0.257	nm
$\bar{K}$	11.4	$\mathrm{W\,m^{-1}\,K^{-1}}$	$a^{\alpha=\beta}$	0.1	–
$\mathbb{C}_{11}$	259.6	GPa	$a^{\alpha\neq\beta}$	0.1	–
$\mathbb{C}_{12}$	179.0	GPa	ρ_0	1.5×10^{6}	mm^{-2}
$\mathbb{C}_{44}$	109.6	GPa	K	10	-
$\mathbb{M}_{11}$	-36.3	$\mathrm{MPa\,K^{-1}}$	y_0	2.57	nm
$\mathbb{M}_{12}$	-16.4	$\mathrm{MPa\,K^{-1}}$	A	1.5×10^{-19}	J
$\mathbb{M}_{44}$	-25.7	$\mathrm{MPa\,K^{-1}}$	η	0.9	–

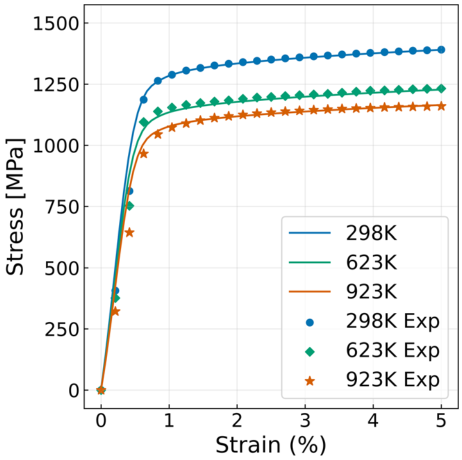

Fig. 2 Average stress–strain response under monotonic mechanical loading at room temperature, at 623K and at 923K for IN718. Experimental data was obtained from Texier et al. [81]

elastic parameters on temperature was taken from Hansen et al. [36], where they characterized them via fits to experimental data on another FCC metal, Cu.

7 Results

7.1 Thermomechanical response of IN718 in uniaxial loading

We start by simulating the stress–strain response under monotonic mechanical loading at room temperature and elevated temperatures, comparing these results directly with experimental curves for the same material. In these simulations, the polycrystal is deformed along the x-axis at room temperature, 623 K, and 923 K up to 5% strain, a strain limit chosen because strains generated during thermal cycling are usually below 5%. Figure 2 shows the resulting stress–strain curves averaged over the RVE. It can be observed that the initial yield stresses, corresponding to the three different temperatures, fall within the approximate range of 1050 to 1250 MPa. Notably, the calculated response shows excellent agreement with the experimental results for IN718 reported by Texier et al. [81] and presented in Fig. 2. This agreement demonstrates the capability of the constitutive model to accurately capture the thermomechanical behavior at constant temperature over a wide range of temperatures. However, it does not guarantee that the same level of accuracy would be achieved during variable temperature loading. We can only note that the mechanical response under thermal cycling conditions remains less explored experimentally, making monotonic loading at different temperatures the best available metric for model validation to date. Next, we will employ the model to understand the evolution of the thermomechanical response solely due to thermal cycling, where neither the temperature nor strain rate remains constant and mechanical deformation is not applied.

7.2 Thermomechanical response in thermal cycling

7.2.1 Time evolution of stress and strain rate

As described in Sect. 6, the polycrystalline material is subjected to a single thermal cycle starting from and returning to room temperature. The thermal cycle is an ideal form of SSTC and in these calculations, no additional boundary conditions of mechanical deformation or stress are imposed. Each thermal cycle is distinguished by its peak temperature amplitude, while the imposed temperature rate is kept fixed at $\dot{\theta} = 1 \times 10^{5}\,\mathrm{K\,s^{-1}}$, a value that falls within the range of typical temperature rates achieved in AM with different manufacturing processes [84]. Four peak amplitudes are considered, leading to temperature differences of $\Delta\theta = 200\,\mathrm{K}$, $\Delta\theta = 350\,\mathrm{K}$, $\Delta\theta = 400\,\mathrm{K}$ and $\Delta\theta = 500\,\mathrm{K}$. These cycles are hereafter referred to as TC200K, TC350K, TC400K and

TC500K, respectively. Figure 3 shows these four thermal cycles, which includes the RVE-average temperature history. The maximum homologous temperature achieved in TC200K, TC350K, TC400K and TC500K cycle is 0.32, 0.42, 0.45 and 0.51, respectively. None of these thermal cycles exceed temperatures where crystallographic slip is no longer the main inelastic deformation mechanism.

Figure 4 presents the stress–strain response averaged over the RVE for the different thermal cycles. It is observed that during TC200K the material remains fully thermoelastic. The absolute maximum stresses achieved is 754 MPa. However, for the greater temperature change experienced in the TC350K cycle, the maximum stress value generated in the material reaches 1073 MPa, close to the elastoplastic transition. It follows then that the thermal cycles with even higher temperature changes, TC400K and TC500K, elicit macroscopic plastic deformation, the latter to an even greater extent, and reach higher peak stresses of 1106 MPa and 1139 MPa respectively. Concomitantly, as the peak temperature increased, the maximum strains along the x-axis achieved at the peak increased from 0.53%, 1.00%, 1.18% and to 1.56%. The maximum strain shows a stronger dependence on the thermal amplitude compared with the maximum stress. This may be expected due to the fact that the geometric effects of thermal expansion are captured by the kinematic formulation and translated into a strong correlation between thermal amplitude and maximum strain, while the effect of thermal expansion on the stress evolution is attenuated due to softening of the elastic moduli and lower hardening due to increased SSD annihilation.

One interesting outcome in every case is that an internally evolving strain rate is generated from the heating and cooling steps imposed in each thermal cycle. The tensorial strain rate field varies appreciably across the material. To compare among the different cycles, however, an average strain rate is computed from the maximum strains depicted in Fig. 4 and the time of each cycle shown in Fig. 3. In the heating step of each cycle, the calculated average strain rate along the x-axis is $2.63\,\mathrm{s}^{-1}$, $2.86\,\mathrm{s}^{-1}$, $2.96\,\mathrm{s}^{-1}$, and $3.12\mathrm{s}^{-1}$, respectively, indicating a clear correlation between the average strain rate and thermal amplitude. Figure 5 further examines the evolution of the strain rate during the heating step. In every case, the strain rate varies substantially over time and the evolving strain rate deviates significantly from its average value. In TC500K, for example, $\dot{\varepsilon}$ rises nearly 50% from its initial value of $2.60\,\mathrm{s}^{-1}$ to $3.80\,\mathrm{s}^{-1}$ at the maximum temperature. The strain rate evolves in the same way among all cycles, with only the end point differing, dictated by the thermal amplitude. Unlike in monotonic mechanical loading, where the strain rate is explicitly controlled and conventionally constant, the strain rate induced during a thermal cycle is neither constant nor explicitly controlled; instead, it is variable and dictated by the heating rate.

7.2.2 Residual stress

Of interest is the residual states of the material left after a thermal cycle has completed. The average stress–strain curve for the thermoelastic cycle, TC200K, would indicate minimal to no bulk residual strains, whereas the curves for the other cycles, TC350K, TC400K and TC500K, would suggest some residual strain left in the material, with the amount increasing with thermal amplitude. Our calculations find that the average residual strains were still non-zero in the TC200K case (0.01%) and moderate for the other cycles, being 0.10%, 0.15% and 0.24%, for TC350K, TC400K and TC500K cycles, respectively. The moderate amount of residual strain observed in all cycles is an indication that there is a pronounced development of reversible thermoelastic strains. Regarding residual stresses, we have seen that even in the low TC200K cycle, the macroscopic thermoelastic response does not rule out the possibility of residual strains and hence also residual stresses. The average residual stress was also low, being 14 MPa (or 1.3% of the yield stress). The corresponding residual stresses left after the higher amplitude cycles are, however, significant. They all fall in the range of hundreds of MPas and increase with the thermal amplitude as well as the level of macroscopic plasticity achieved during the cycle. Specifically, the average residual stress obtained for each individual cycle from TC350K to TC500K was 292 MPa, 440 MPa and 720 MPa, respectively. These average stresses correspond to 26.6%, 40.0% and 65.5% of the yield stress of this material.

Figure 6 presents the residual VON MISES stress maps calculated at cut C_x (see Fig. 1) for each cycle. These cuts are representative and consistent throughout the entire RVE. The stress distribution in all cases is notably heterogeneous in spite of the fact that the thermal expansion coefficients are isotropic and the temperature at any given cross section is constant. The main effect seen is that larger microscale residual stresses result from cycles with greater thermal amplitudes. Although the macroscopic stress–strain curve for the lowest amplitude cycle, TC200K, remained in the elastic regime, a heterogeneous distribution of residual stresses still develops at the microscale. In the case of a greater amplitude cycle of TC350K, the material experiences some plastic deformation, albeit of limited extent. Yet, the residual stresses are still significant, with stress hotspots nearing 700 MPa. As the thermal amplitude increases and the material manifests bulk plasticity, the residual stresses not only increase accordingly, but also follow a similar pattern in their residual stress distributions as those in the lower amplitude cycles. This pattern is characterized by stress hotspots at specific grains, occasionally contrasting with the surrounding grains exhibiting substantially lower residual stresses. Stress concentration at grain boundaries and triple junctions of highly stressed grains, are also observed; some of these are highlighted in

Fig. 3 Average temperature history for thermal cycles starting from and returning to room temperature featuring different thermal amplitudes: TC200K, TC350K, TC400K and TC500K. Timescale corresponds to the temperature rate of $1 \times 10^5 \mathrm{K\,s^{-1}}$

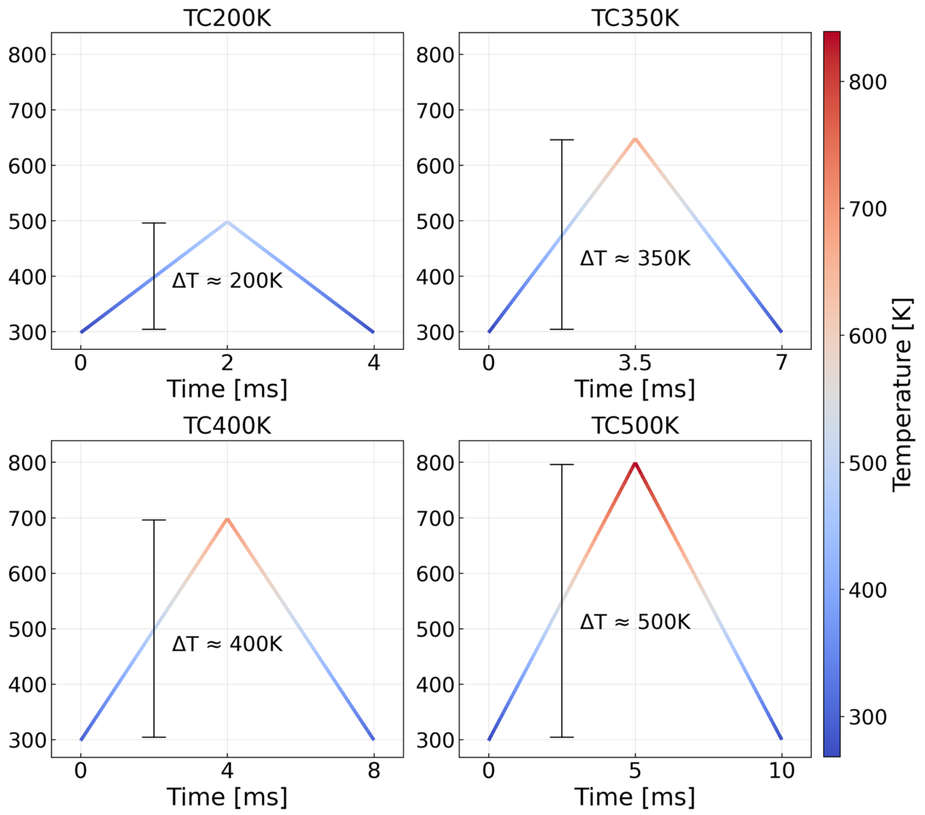

Fig. 4 Average stress–strain response induced by the thermal cycles TC200K, TC350K, TC400K and TC500K (see Fig. 3) evoking different regimes of deformation

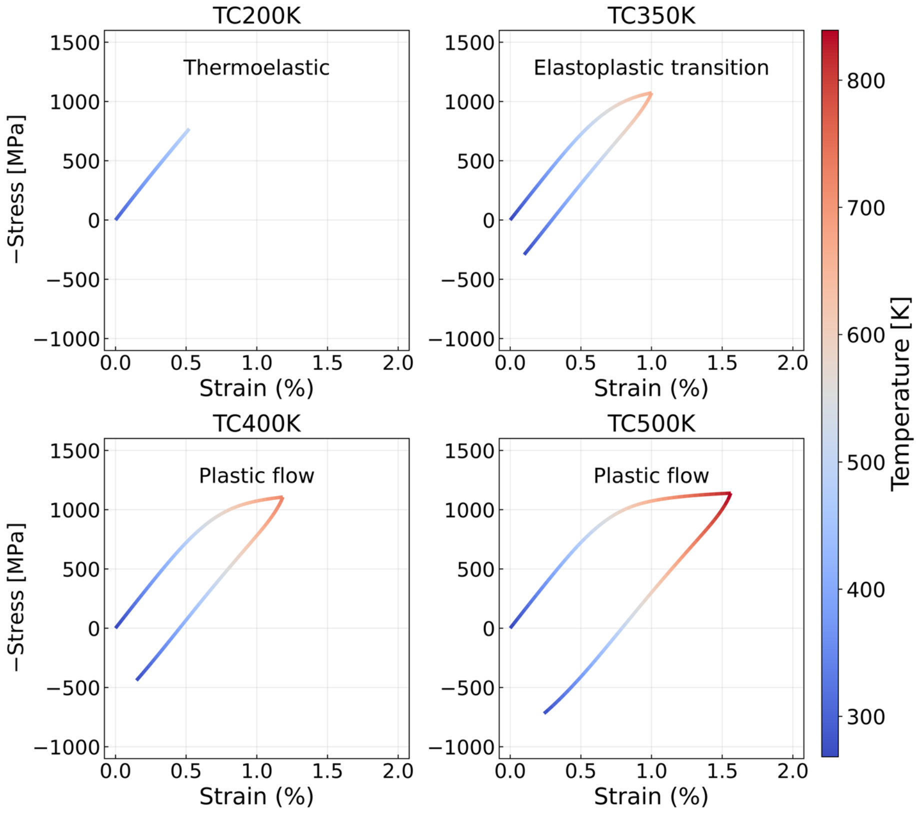

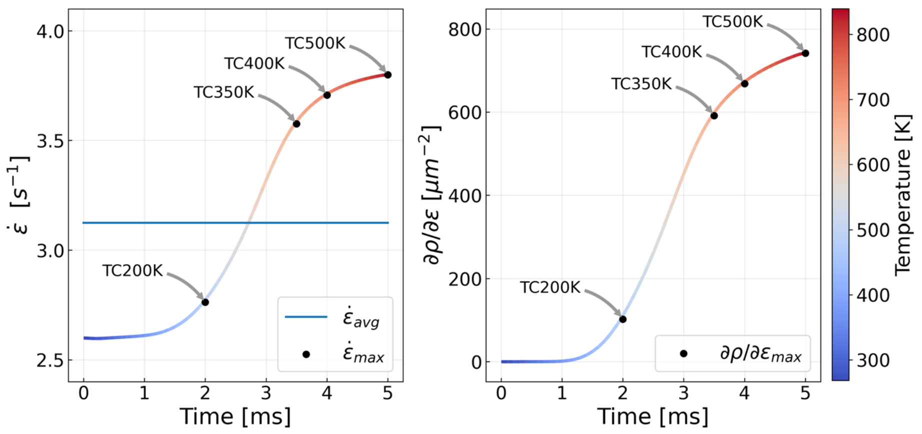

Fig. 5 Evolution of the strain rate during the heating step (left) with average value for TC500K indicated in the plot. Evolution of the total SSD density gradient during the heating step (right)

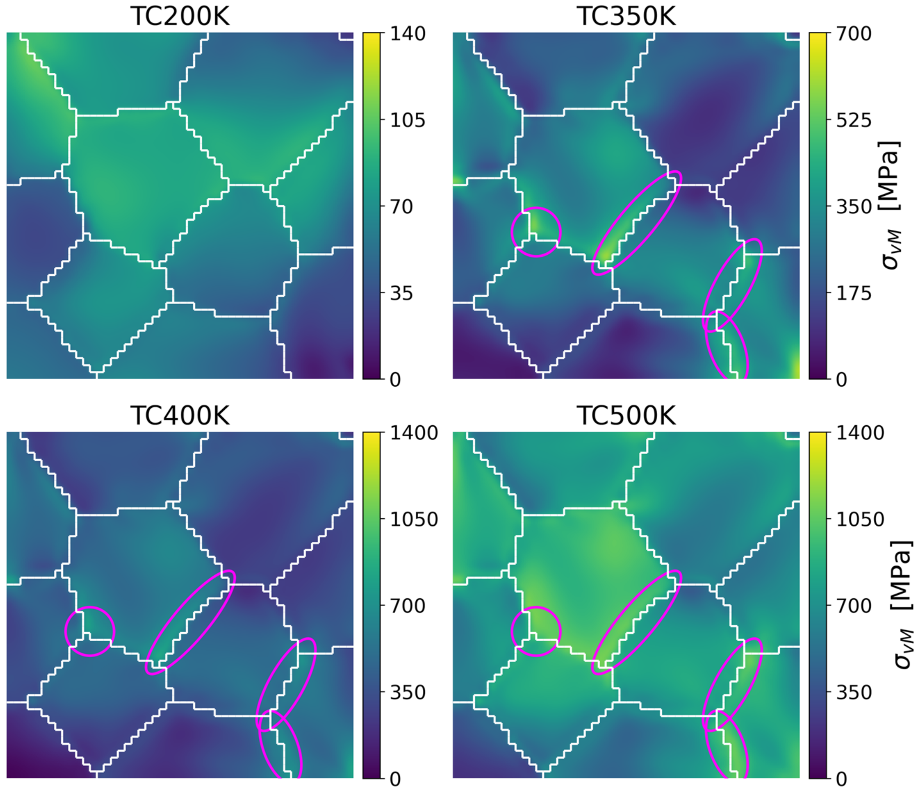

Fig. 6 Comparison between the residual von Mises stress distribution under different thermal amplitudes. Highlighted circles indicate stress hotspots at regions of the microstructure featuring grain boundaries and/or triple junctions. Cut C_x perpendicular to the x-axis at mid-height (see Fig. 1)

Fig. 6. Altogether, these observations indicate that in addition to the thermomechanical variables of thermal amplitude and temperature rate, the features and constraints of the granular microstructure play a significant role in the residual stress distribution.

7.2.3 Residual SSD density

An initial SSD density was homogeneously assigned to all slip systems (see Table 1) and thus the total initial value is $\rho_{\text{total}} = 18\,\mu\text{m}^{-2}$. Figure 7 presents the time evolution of the total SSD density averaged over the RVE for each thermal cycle. The results show that the thermal cycling alone with amplitudes over 350K was sufficient to induce an increase in the SSD density, resulting in residual stored dislocations even for TC350K, which just reached the elasto-plastic transition point. The uptick in the total stored density identified at the end of TC500K is worth noting. It shows that even the cooling step might elicit macroscopic plastic deformation, provided that the thermal amplitude is sufficiently high, underscoring the sensitivity of the SSD density to thermal cycling conditions.

We also note that the developing and rising strain rate seen in Fig. 5 becomes noticeable between 1 and 2 ms, which coincides with the time $\partial\rho/\partial\varepsilon$ starts actively evolving. At this point in time, macroscopic yield has not yet occurred in Fig. 4. In fact, it is observed even for the macroscopic thermoelastic cycle, TC200K. The uptick in $\partial\rho/\partial\varepsilon$ is an indication

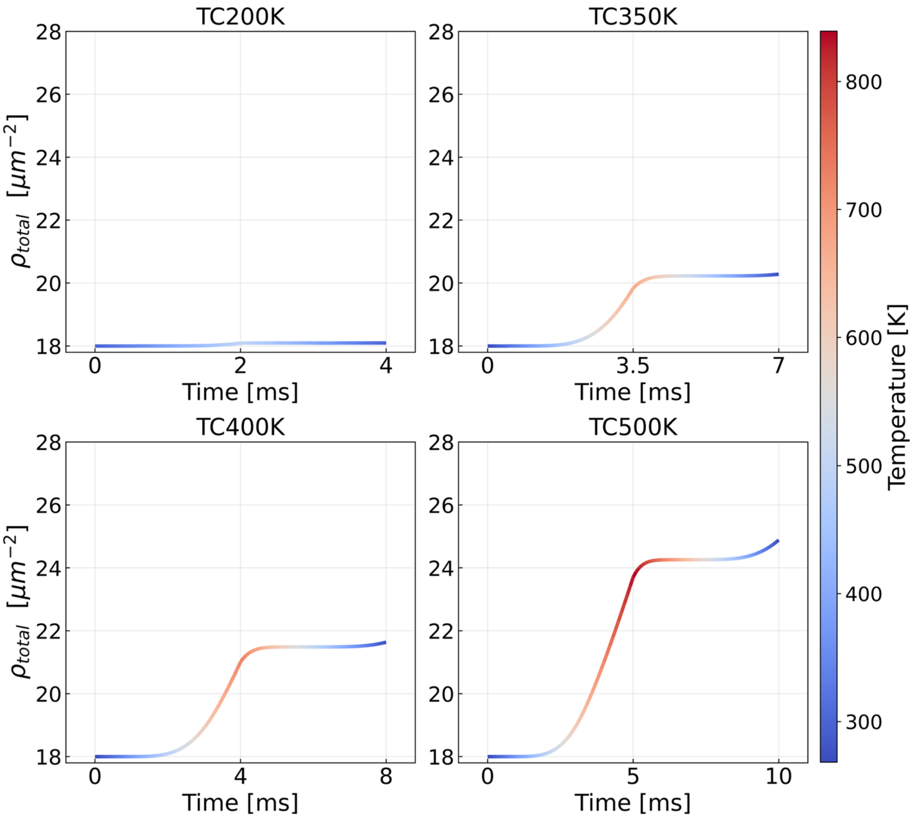

Fig. 7 Average SSD evolution for each thermal cycle shown in Fig. 3. For thermal amplitudes of 350 K and above, thermal cycling alone can induce an increase in the SSD density. Timescale corresponds to the temperature rate of $1 \times 10^5\,\mathrm{K\,s^{-1}}$

of microplasticity taking place at early stages of thermal cycling. It further suggests that the partially constrained thermal expansion is sufficient to induce microplasticity even under macroscopic thermoelastic conditions.

Figure 8 shows the residual SSD density maps calculated at cut C_x (see Fig. 1) for each cycle. Following the trend observed in Fig. 7, the thermal amplitude experienced during the cycle is directly associated with the increase in the SSD density. Consistent with the average SSD evolution, the thermoelastic cycle did not lead to distinguishable dislocation storage. Conversely, TC500K, which reached bulk plasticity, shows not only higher SSD density, but a rather heterogeneous distribution. In fact, the residual SSD density shows a stronger dependence on the microstructural constraints when compared with the residual stress distribution. As highlighted in the map, SSD density hotspots are associated microstructural features such as grain boundaries or triple junctions. Such microstructurally driven localization of SSD density occurs in all cross sections of the 3D volume.

7.2.4 Residual lattice rotation

Figure 9 presents the residual lattice rotation maps calculated at cut C_x (see Fig. 1) remaining after each thermal cycle. The in-plane rotations shown are mapped for comparison among the cycles but we note that these rotations developed with full constraints from the 3D bulk. With the thermal cycling alone, a meaningful degree of lattice rotation develops in grains that were initially uniform in orientation. The intragranular rotations span from $-0.4°$ to $0.4°$, for the higher thermal amplitudes cycles. Similarly to the previous micromechanical field variables, the lattice rotations increase with the thermal amplitude. However, different patterns of heterogeneity can be seen in its spatial distribution. For instance, some grains, like grains 1, 2 and 4 (highlighted in Fig. 9), develop large rotations but limited grain-spanning intragranular rotation gradients. In these grains, significant lattice rotation gradients developed instead in at least one of their grain boundaries. Conversely, grains, such as grains 3, 5, 6 and 7, develop notable short-range intragranular rotation gradients, indicating a change in the sign of the lattice rotation angle within the grain.

Considering that slip activity is the main driving factor for lattice rotation, a closer look at the activated slip systems is taken. Figure 10 shows the contribution of the most activated slip systems to the total slip for grains with minimal intragranular lattice rotation gradients in TC500K. Some grains, such as grains 1 and 4 shown, represent those with low intragranular rotation gradients. In these grains, there is a clearly predominant slip system activated, accounting for the majority of the total slip. We found this to be the case for grains that developed low intragranular rotation gradients consistent throughout the microstructure and exemplified here through these specific grains. For grain 1, the minimal

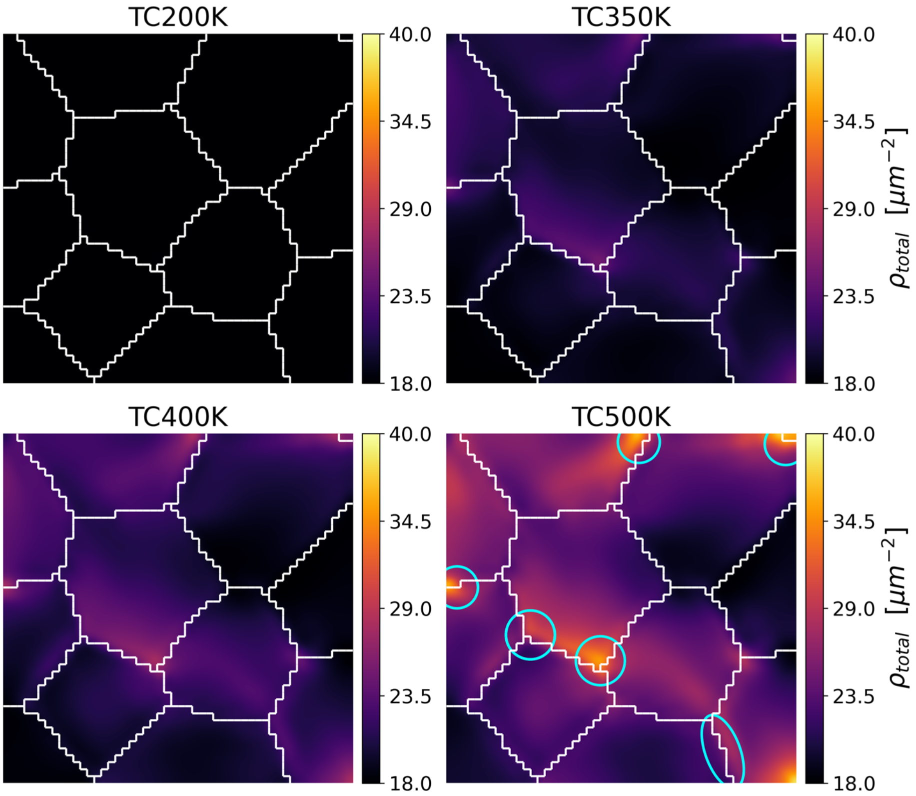

Fig. 8 Comparison between the residual SSD density distribution under different thermal amplitudes. Highlighted circles indicate SSD density hotspots at regions of the microstructure featuring grain boundaries and/or triple junctions. Cut C_x perpendicular to the x-axis at mid-height (see Fig. 1)

gradient observed in its right-most region is associated with a partial change from a predominant C5 slip to a shared C5/C1 slip. This is a mild change as C5 remains active, resulting in an attenuated rotation gradient, without sign change. For grain 4, B4 slip accounts for the majority of slip throughout the grain. The mild change in lattice orientation seen in Fig. 9, without sign change, coincides with the regions where A3 and B4 slip interchange.

Conversely, Fig. 11 shows the contribution of the most activated slip systems to the total slip for a few exemplar grains with significant intragranular lattice rotation gradients. Multi-slip activation (three or more slip systems) is predicted in grains that exhibit marked short-range intragranular gradients. For grain 3, the B4 system remains active throughout the entire grain and accommodates part of the total slip. However, the B5 and C1 slip systems are also activated in different regions of the grain. Furthermore, the region where a change in lattice rotation sign is observed in grain 3 in Fig. 9 coincides with the region where B5 changes into C1 in Fig. 11. A similar assessment can be made for grain 5, where C3 slip is present throughout the grain, but B2 and C1 are also activated in different regions. In particular, the lower portion of the grain where there is a transition between B2 and C1, is the region where a significant short range gradient, with change in lattice rotation sign, is observed.

7.2.5 Multicycle response

We assess the mechanical response under multiple successive thermal cycles. Figure 12 shows the RVE-average temperature (left) when TC500K, TC400K, and TC350K are applied sequentially. The average stress–strain behavior, shown in Fig. 12 (center), can be compared to that observed when each cycle is applied individually. Specifically, while the response of the first cycle is identical to the individual TC500K, the subsequent cycles differ significantly. When applied separately, TC400K reaches macroscopic plastic flow, and TC350K reaches the elasto-plastic transition, as presented in Fig. 4. However, when these cycles follow TC500K, they both remain in the thermoelastic regime. TC350K and TC400K reach maximum compressive stresses of 1070 MPa and 1100 MPa, respectively, when applied as stand-alone cycles, but only about 650 MPa and 800 MPa in the multicycle regime. Additionally, the final residual stress remains unchanged by the subsequent cycles and is fully defined by the thermal cycle with the highest amplitude. Finally, the difference between the SSD density obtained with TC500K and the multicycle is shown in Fig. 12 (right). The maximum percentile difference is 5%, indicating that the dislocation activity elicited by the subsequent cycles is minimal and restricted to regions with microstructural constraints in the most stressed grains.

Fig. 9 Comparison between the residual lattice rotation under different thermal amplitudes. Grains 1, 2, and 4 show significant rotation with limited intragranular rotation gradients, whereas grains 3, 5, 6, and 7 are characterized by notable short-range rotation gradients. Cut C_x perpendicular to the x-axis at mid-height (see Fig. 1)

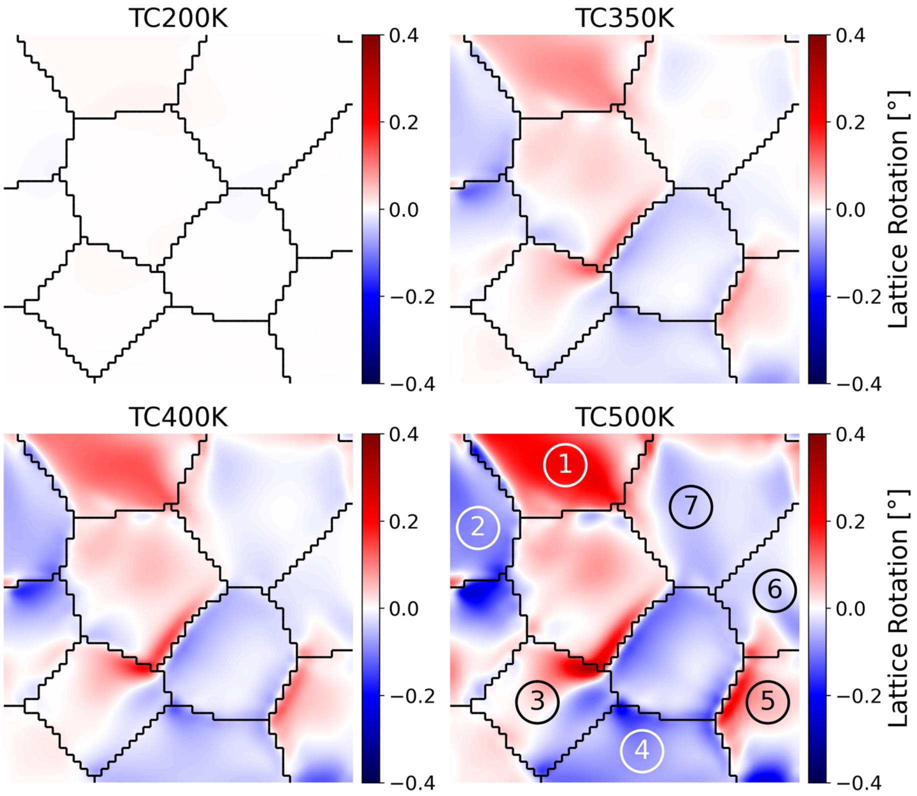

Fig. 10 Contribution of the three most active slip systems to the total slip for grains with minimal intragranular lattice rotation gradient in TC500K. Remaining slip systems were not activated or the total accumulated slip was minimal. See Table 2 for the designation of the slip systems

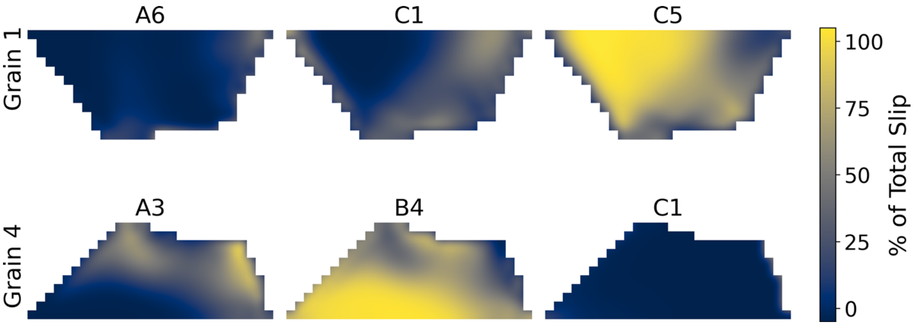

Fig. 11 Contribution of the three most active slip systems to the total slip for grains with substantial intragranular lattice rotation gradient in TC500K. Remaining slip systems were not activated or the total accumulated slip was minimal See Table 2 for the designation of the slip systems

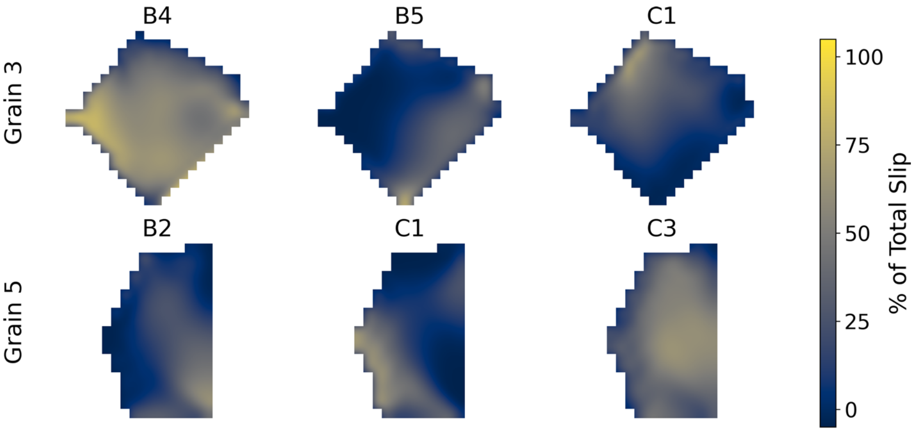

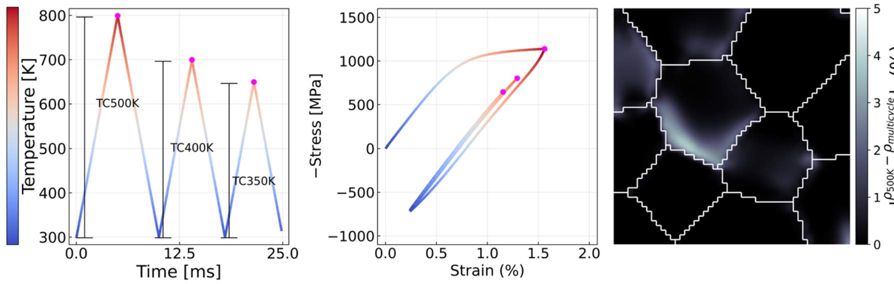

Fig. 12 Average temperature history for subsequent thermal cycles starting from and returning to room temperature (left). Average stress–strain response induced by the multiple thermal cycles (center). Comparison between the resulting SSD density due to TC500K alone and multiple successive cycles (right)

8 Discussion

From a length scale perspective, residual stresses are usually classified as macroscale and microscale residual stresses [13, 22, 88]. The microscale stress maps, i.e. stresses that vary within the grain scale, were presented in Fig. 6, while the average stress response is shown in Fig. 4. Except for the thermoelastic cycle, our results indicate high residual stresses, in the range of hundreds of MPas at the end of every other thermal cycle. The residual stresses exhibit a strong dependence on the thermal amplitude. In fact, these observations conform with the results presented by Lindroos et al. [53], Grilli et al. [35] and Hu et al. [43] where residual stresses at the order of hundreds of MPas were predicted through CP simulations, the first on H13 tool steel and the last two on 316 L stainless steel. Additionally, component level residual stresses on lower deposition layers were calculated by Singh et al. [76] on IN718 reaching up to 750 MPa while Nadammal et al. [66] measured residual stresses ranging from 0 to 400 MPa varying with the scanning strategy. While we note that the modeling frameworks across these studies, as well as in our own, differ significantly, the overarching trend is closely aligned.

It should be highlighted that the average stress–strain response shown in Fig. 4 is consistent with the response delineated by the temperature gradient mechanism (TGM) [5, 48, 63]. According to the TGM model, the thermal expansion of heated material, surrounded by material at lower temperature, leads to compressive stresses during the heating step. During the cooling step, the plastic strains developed in the heating phase partially counteract the thermal shrinkage, resulting in tensile stresses. This is precisely the behavior observed in Fig. 4. Moreover, the higher the thermal amplitude, the greater the plastic strains, which lead to higher tensile residual stresses at the end of the thermal cycle. The TGM adequately explains the strong connection between thermal amplitude and the magnitude of residual stresses. While our results confirm that RVE-based CP simulations can provide a pathway for calculating residual stresses and intragranular misorientations that develop in AM, we acknowledge that the current set up and boundary conditions are a simplification of the complex process surrounding AM. First, the constitutive model considers thermally activated slip without grain boundary motion or deformation. Thus, the model applies to several layers below the surface, where peak temperatures during AM processes are low (below $0.5T_{melt}$). Second, the current application also considers for the most part a single thermal cycle, whereas a series of thermal cycles varying in peak temperature and rates are involved in AM processes. Future research should focus on these aspects to enhance the model's applicability to more realistic AM scenarios. Finally, the present RVEs contain several grains nearly equiaxed in shape. Solidified structures from AM processes can have long columnar shapes. Many of these limitations can be lifted when the aim is to apply the current approach to AM processing. It would provide a potential alternative to conventional approaches requiring large-volume representations in slab-shaped models, which generally depend on significantly simplified constitutive models to manage computational demands in large-scale simulations.

Figure 6 shows the residual stress maps for different thermal amplitudes. The strong heterogeneity of the inter and intra-granular stress distribution aligns with the expected distribution of microscale residual stresses [88], and is also reflected in the spatial fluctuations experimentally observed by Liu et al. [54] on laser rapid formed IN718 at a coarser spatial resolution, where residual stresses ranged from 0 to a maximum of 650MPa. The heterogeneity of the stress distribution, despite the isotropic nature of the thermal expansion deformation gradient is attributable, at a significant extent, to the anisotropic elastic response of the material. The effect of elastic anisotropy on the distribution of microscale residual stresses is particularly significant given the limited level of bulk plasticity induced by the thermal cycles. Figure 13 shows how the residual VON MISES stress distribution becomes less heterogeneous as the Zener ratio is reduced to 1. Specifically, the residual stress distribution of the thermoelastic cycle, TC200K, becomes homogeneous, while the residual stress distribution of TC500K, that undergoes bulk plastic flow, has its heterogeneity significantly reduced.

It is immediate from Fig. 5 that the strain rate is not constant, but evolves with the thermal cycles. In fact, it strongly resembles the evolution of the SSD density gradient. This can be explained by the interplay between the thermal expansion, kinematically captured by $\boldsymbol{F}^{\theta}$, and the non-linear macroscopic plastic deformation, kinematically described by $\boldsymbol{F}^{\mathrm{p}}$, resulting in a varying $\dot{\boldsymbol{F}}$. Furthermore, we observed that the amplitude of the strain rate evolution is dependent on the thermal amplitude. For our thermal cycle with the highest amplitude, TC500K, $\dot{\varepsilon}$ exhibits a growth of nearly 50% from its initial value. Cycles with even higher thermal amplitudes, which are certainly attainable during SSTC, would likely lead to even higher amplitudes on the strain rate evolution. Such new observation points to the complexity of the deformation conditions imposed by SSTCs as the microstructure experiences evolving strain rates. We also note that while the temperature rise from inelastic heat generation, $\dot{Q}$, is only approximately 1.5 K in TC500K-a minute increase-its contribution is retained in the model formulation for completeness. Its inclusion also ensures accuracy across a broader range of scenarios, potentially involving higher strain rates as a result of higher temperature rates. Materials with higher melting points, for instance, might be subject to greater thermal amplitudes and consequently more substantial plastic deformation and inelastic heating.

Figures 7 and 8 explore the residual SSD density both in an average sense throughout each cycle and at the residual state. Our calculations show that thermal cycling can induce meaningful dislocation density evolution, even in the absence of substantial macroscopic plastic deformation. These results conform with findings from Bertsch et al. [7] and Wang et al. [85], respectively, that reported on the influence of both thermal cycling and residual stresses on the dislocation density evolution. Furthermore, the heterogeneity of the SSD density maps observed in Fig. 8, exhibiting regions of high and low SSD density, is well aligned with recent observations made by Hu et al. [44]. Therefore, we first emphasize that SSD density evolution is possible from thermal cycling alone. Furthermore, we note that the SSD density evolution obtained through thermal cycling, albeit lower, can be in the same order of magnitude of that obtained through mechanical loading. Finally, we observe that dislocation annihilation bears significant influence on the total SSD density due to the higher temperatures.

Analysis of the calculations, showcased in Fig. 9, reveals a notable development of residual lattice rotation due to thermal cycling, which intensifies with increased thermal amplitude. Due to the imposed loading conditions, it is observed that there is no net rotation overall, as the average rotation angle remains at 0°. However, the lattice rotation fields are highly heterogeneous, with local rotation angles reaching up to ±0.4°. This lattice rotation resulting from thermal cycling, is likely to compound with rotation induced by subsequent mechanical loading, thereby significantly influencing mechanical behavior under service conditions. Indeed, at the grain level, properties such as lattice orientation are crucial for predicting failure mechanisms, including crack formation due to localized slip bands [9, 38, 78]. While this paper does not specifically address the evolution of GND density, it is noteworthy that lattice rotation fields are often accompanied by GND density development [21, 24, 80]. Consequently, our results suggest the emergence of an additional dislocation density population attributable to thermal cycling.

Finally, Fig. 12 explored the differences observed between the individual thermal cycles and the multicycle response, which can be attributed to two primary factors. First, the initial thermal cycle (TC500K) has expanded the yield locus of the material, resulting in an increased yield stress. This higher yield stress is challenging to achieve with the lower amplitude subsequent cycles (TC400K and TC350K), which partially explains why their response remains in the thermoelastic regime when applied after TC500K. Second, the subsequent cycles begin in an elastic tensile stress state, as a consequence of the first cycle (TC500K), and must first transition to the compressive regime. This transition requires overcoming the pre-existing tensile stress, further limiting the ability of these cycles to induce significant compressive plastic deformation. Consequently, the compressive stresses and dislocation activity in the multicycle regime are markedly reduced compared to when the cycles are applied individually. These factors together could explain the reduced peak stresses and minimal dislocation activity observed in the multicycle experiments and highlight the notable importance of the first thermal cycle with highest amplitude.

9 Conclusions

In this work, we presented a fully coupled thermomechanical CP framework. The formulation features thermal sensitivity through the kinematic description, the single crystal constitutive law and the coupled governing equations. We applied this framework to IN718 which shows an initial flow stress of 1100MPa. The model was employed to study the evolution and formation of residual stresses, SSD density and lattice rotation originating from thermal cycling with different thermal amplitudes, namely $\Delta\theta = 200$K, $\Delta\theta = 350$K, $\Delta\theta = 400$K and $\Delta\theta = 500$K. The mechanical response elicited under partially constrained thermal expansion was evaluated.

The thermal amplitude was a key factor in defining the level of plastic deformation evoked by a given cycle. In fact, the deformation regime achieved in each cycle, thermoelastic (TC200K), elastoplastic transition (TC350K) and bulk plasticity (TC400K and TC500K) was defined by the imposed thermal amplitude. The magnitude of the residual stresses, in the order of hundreds of MPas, except for TC200K, was also strongly dependent on the thermal amplitude. The average residual stress in each cycle reached 1.3%, 26.6%, 40.0%

Fig. 13 Comparison between the residual VON MISES stress distribution under anisotropic (left) and isotropic (right) elastic response. Thermal amplitudes of $\Delta\theta = 200\,\mathrm{K}$ and $\Delta\theta = 500\,\mathrm{K}$. Cut C_x perpendicular to the x-axis at mid-height (see Fig. 1)

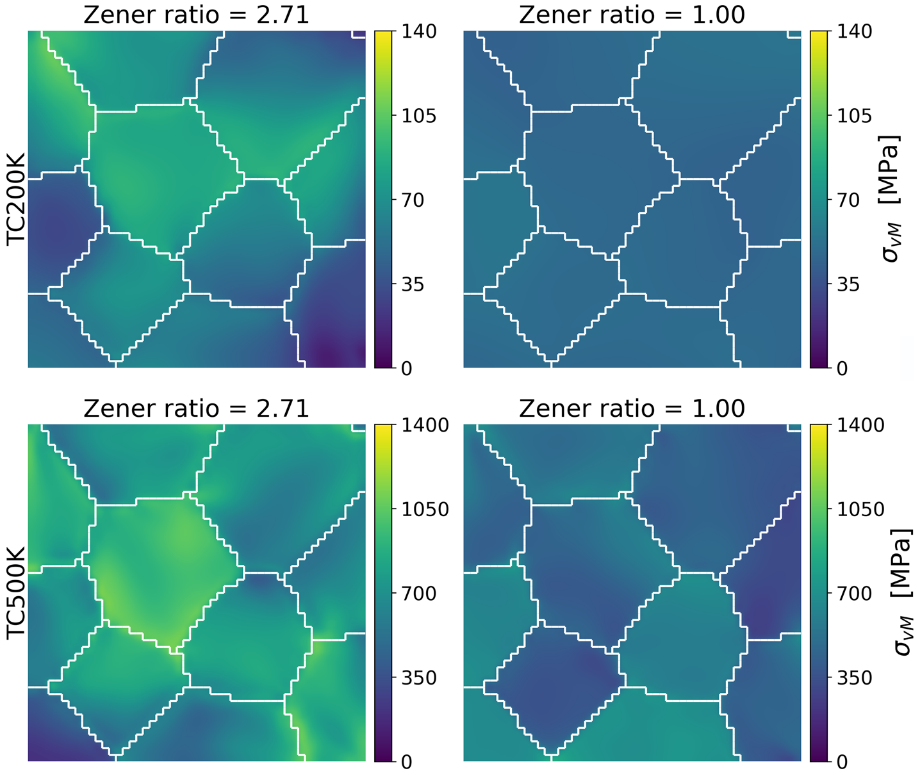

and 65.5% of the yield stress, respectively. Our calculations showed, for the first time, the evolving strain rate due to thermal cycling. We further noticed microplasticity taking place at early stages of thermal cycling, evidenced by the positive dislocation storage rate and residual stresses, even in the macroscopic thermoelastic regime. The influence of elastic anisotropy on the heterogeneity of the residual stress distribution was demonstrated to be significant. We also demonstrated that thermal cycling alone can be enough to provoke SSD density evolution, particularly at regions with microstructural constraints such as grain boundaries and triple junctions. We calculated lattice rotation obtained from thermal cycling ranging from ±0.4° and associated the intragranular lattice rotation gradients with local changes in predominant slip systems. Finally, the simulations show predominant influence of the cycle with the highest thermal amplitude when the material experiences multiple successive cycles. The final state of residual stresses, SSD density and lattice rotation are all evidently set by the highest temperature cycle.

Appendix A

The single crystal constitutive model described in Sect. 3 was implemented in a user-defined material subroutine (UMAT) in Abaqus/Standard. The simulations were carried out in fully coupled thermal-stress analyses with fully integrated hexahedral elements featuring both displacement and temperature degrees of freedom (C3D8T). In order to achieve convergence, the Newton–Raphson scheme requires the definition of four distinct Jacobians. These will be represented here by $\mathbb{W}^{\boldsymbol{\sigma},\boldsymbol{E}}$, $\mathbb{W}^{\boldsymbol{\sigma},\theta}$, $\mathbb{W}^{\dot{Q},\boldsymbol{E}}$ and $\mathbb{W}^{\dot{Q},\theta}$ denoting tensors of rank 4, 2, 2 and 0 respectively. In the following subsections, the analytical calculation and algorithmic implementation of each one will be outlined. The derivation of $\mathbb{W}^{\boldsymbol{\sigma},\boldsymbol{E}}$ advances the procedure initially set forth by Dai [17] and Balasubramanian [4] to include the thermal-expansion kinematics presented in Sect. 2. The analytical derivation of $\mathbb{W}^{\boldsymbol{\sigma},\theta}$, $\mathbb{W}^{\dot{Q},\boldsymbol{E}}$ and $\mathbb{W}^{\dot{Q},\theta}$ within a classical single crystal constitutive framework is presented here for the first time.

The notation $t_n = t$ and $t_{n+1} = t + \Delta t$ is used to represent the beginning and the end of an arbitrary time interval $[t_n, t_{n+1}]$. All quantities are evaluated at t_{n+1}, unless explicitly specified.

Mechanical Jacobian: $\mathbb{W}^{\boldsymbol{\sigma},\boldsymbol{E}}$

The mechanical Jacobian matrix used in the implicit backward Euler integration scheme is defined as:

$$\mathbb{W}^{\boldsymbol{\sigma},\boldsymbol{E}} = \frac{\partial \boldsymbol{\sigma}}{\partial \boldsymbol{E}_t}, \tag{30}$$

where $\boldsymbol{E}$ denotes the relative symmetric strain tensor, which can be approximated by:

$$\boldsymbol{E}_t = \ln \boldsymbol{U}_t \approx \boldsymbol{U}_t - \boldsymbol{I} \Rightarrow \partial \boldsymbol{E}_t \approx \partial \boldsymbol{U}_t, \tag{31}$$

with $\boldsymbol{U}$ representing the relative right stretch tensor. The mechanical Jacobian is then approximated by:

$$\mathbb{W}^{\boldsymbol{\sigma},\boldsymbol{E}} \approx \frac{\partial \boldsymbol{\sigma}}{\partial \boldsymbol{U}_t}. \tag{32}$$

From Equation (10), the CAUCHY stress tensor takes the following form in index notation:

$$\sigma_{ij} = \frac{1}{\det \boldsymbol{F}^{\mathrm{e}}} \left(F^{\mathrm{e}}_{im} S_{mn} F^{\mathrm{eT}}_{nj} \right), \tag{33}$$

therefore,

$$\begin{aligned} \mathbb{W}^{\boldsymbol{\sigma},\boldsymbol{E}}_{ijkl} = \frac{1}{\det \boldsymbol{F}^{\mathrm{e}}} \Big[& \mathcal{T}_{imkl} S_{mn} F^{\mathrm{eT}}_{nj} \\ & + F^{\mathrm{e}}_{im} \mathcal{Q}_{mnkl} F^{\mathrm{eT}}_{nj} + F^{\mathrm{e}}_{im} S_{mn} \mathcal{T}_{jnkl} \\ & - F^{\mathrm{e}}_{im} S_{mn} F^{\mathrm{eT}}_{nj} \mathcal{T}_{pqkl} F^{\mathrm{e}-1}_{qp} \Big], \end{aligned} \tag{34}$$

where,

$$\mathcal{T}_{ijkl} = \frac{\partial F^{\mathrm{e}}_{ij}}{\partial U_{kl}} \quad \text{and} \quad \mathcal{Q}_{ijkl} = \frac{\partial S_{ij}}{\partial U_{kl}}. \tag{35}$$

9.0.6 Calculation of $\mathcal{T}_{ijkl}$

We begin with the definitions of the relative deformation gradient as well as its polar decomposition, precisely:

$$\boldsymbol{F}_t = \boldsymbol{F}\boldsymbol{F}^{-1}(t_n), \tag{36a}$$

$$\boldsymbol{F}_t = \boldsymbol{R}_t \boldsymbol{U}_t. \tag{36b}$$

The elastic deformation gradient is then expressed by:

$$\begin{aligned} \boldsymbol{F}^{\mathrm{e}} &= \boldsymbol{F}\boldsymbol{F}^{\theta^{-1}}\boldsymbol{F}^{\mathrm{p}^{-1}} = \boldsymbol{F}_t \boldsymbol{F}(t_n) \boldsymbol{F}^{\theta^{-1}} \boldsymbol{F}^{\mathrm{p}^{-1}} \\ &= \boldsymbol{R}_t \boldsymbol{U}_t \boldsymbol{F}^{\mathrm{e}}(t_n) \boldsymbol{F}^{\mathrm{p}}(t_n) \boldsymbol{F}^{\theta}(t_n) \boldsymbol{F}^{\theta^{-1}} \boldsymbol{F}^{\mathrm{p}^{-1}}. \end{aligned} \tag{37}$$

We recall Equations (20b) and (21b), respectively:

$$\boldsymbol{F}^{\theta^{-1}} \approx \boldsymbol{F}^{\theta^{-1}}(t_n) \left(\boldsymbol{I} - \Delta\theta \boldsymbol{\beta} \right), \tag{38a}$$

$$\boldsymbol{F}^{\mathrm{p}^{-1}} \approx \boldsymbol{F}^{\mathrm{p}^{-1}}(t_n) \left(\boldsymbol{I} - \sum_{\alpha} \Delta\gamma^{\alpha} \boldsymbol{S}^{\alpha}_{0} \right). \tag{38b}$$

Substituting these in Equation (37) yields:

$$\boldsymbol{F}^{\mathrm{e}} = \boldsymbol{R}_t \boldsymbol{U}_t \boldsymbol{F}^{\mathrm{e}}(t_n) \boldsymbol{K}(t_n) - \boldsymbol{R}_t \boldsymbol{U}_t \boldsymbol{F}^{\mathrm{e}}_t \boldsymbol{K}(t_n) \sum_{\alpha} \Delta\gamma^{\alpha} \boldsymbol{S}^{\alpha}_{0}, \tag{39}$$

where $\boldsymbol{K}(t_n) = \boldsymbol{F}^{\mathrm{p}}(t_n) \left(\boldsymbol{I} - \Delta\theta \boldsymbol{\beta} \right) \boldsymbol{F}^{\mathrm{p}^{-1}}(t_n)$. Finally, $\mathcal{T}_{ijkl}$ is given by:

$$\begin{aligned} \mathcal{T}_{ijkl} = & R_{ik} F^{\mathrm{e}}_{lp}(t_n) K_{pj}(t_n) \\ & - R_{ik} F^{\mathrm{e}}_{lp}(t_n) K_{pq}(t_n) \sum_{\alpha} \Delta\gamma^{\alpha} S^{\alpha}_{0,qj} \\ & - R_{im} U_{mn} F^{\mathrm{e}}_{np}(t_n) K_{pq}(t_n) \sum_{\alpha} J^{\alpha}_{kl} S^{\alpha}_{0,qj}, \end{aligned} \tag{40}$$

with,

$$J^{\alpha}_{ij} = \frac{\partial \Delta\gamma^{\alpha}}{\partial U_{ij}}. \tag{41}$$

9.0.7 Calculation of $\mathcal{Q}_{ijkl}$

The $\mathcal{Q}_{ijkl}$ tensor is calculated from Eq. (26) as:

$$\mathcal{Q}_{ijlk} = \frac{\partial S_{ij}}{\partial U_{kl}} = \mathcal{D}_{ijkl} - \sum_{\alpha} C^{\alpha}_{ij} J^{\alpha}_{kl} - \sum_{\alpha} \Delta\gamma^{\alpha} \Gamma^{\alpha}_{ijkl}, \tag{42}$$

where,

$$\mathcal{D}_{ijkl} = \frac{\partial S^{\mathrm{tr}}_{ij}}{\partial U_{kl}}, \tag{43a}$$

$$\Gamma^{\alpha}_{ijkl} = \frac{\partial C^{\alpha}_{ij}}{\partial U_{kl}}, \tag{43b}$$

from Eq. (27a), we have:

$$S^{\mathrm{tr}}_{ij} = \frac{1}{2} \mathbb{C}_{ijmn} \left(A_{mn} - \delta_{mn} \right) \Rightarrow \frac{\partial S^{\mathrm{tr}}_{ij}}{\partial U_{kl}} = \frac{1}{2} \mathbb{C}_{ijmn} \mathcal{E}_{mnkl}, \tag{44}$$

hence,

$$\mathcal{D}_{ijkl} = \frac{1}{2} \mathbb{C}_{ijmn} \mathcal{E}_{mnkl}, \tag{45}$$

with,

$$\mathcal{E}_{ijkl} = \frac{\partial A_{ij}}{\partial U_{kl}}, \tag{46}$$

which is obtained from Eq. (24) as:

$$\begin{aligned} \mathcal{E}_{ijkl} = & F^{\mathrm{p}-\mathrm{T}}_{im}(t_n) \Theta_{mn} F^{\mathrm{pT}}_{np}(t_n) F^{\mathrm{eT}}_{pq}(t_n) U_{qk} \\ & F^{\mathrm{e}}_{lr}(t_n) F^{\mathrm{p}}_{rv}(t_n) \Theta_{vu} F^{\mathrm{p}-1}_{uj}(t_n) \\ & + F^{\mathrm{p}-\mathrm{T}}_{im}(t_n) \Theta_{mn} F^{\mathrm{pT}}_{np}(t_n) F^{\mathrm{eT}}_{pk}(t_n) U_{lw} \\ & F^{\mathrm{e}}_{wr}(t_n) F^{\mathrm{p}}_{rv}(t_n) \Theta_{vu} F^{\mathrm{p}-1}_{uj}(t_n), \end{aligned} \tag{47}$$

where,

$$\Theta_{ij} = \delta_{ij} - \Delta\theta\beta_{ij}. \tag{48}$$

Equation (43b) is calculated from Eq. (27b), precisely:

$$\Gamma^{\alpha}_{ijkl} = \frac{\partial C^{\alpha}_{ij}}{\partial U_{kl}} = \frac{1}{2}\mathbb{C}_{ijmn}\left(S^{\alpha\,\mathrm{T}}_{0,mp}\frac{\partial A_{pn}}{\partial U_{kl}} + \frac{\partial A_{mp}}{\partial U_{kl}}S^{\alpha}_{0,pn}\right), \tag{49}$$

and therefore,

$$\Gamma^{\alpha}_{ijkl} = \frac{1}{2}\mathbb{C}_{ijmn}\left(S^{\alpha\,\mathrm{T}}_{0,mp}\mathcal{E}_{pnkl} + \mathcal{E}_{mpkl}S^{\alpha}_{0,pn}\right). \tag{50}$$

We proceed to the calculation of J^{α} with the following simplification:

$$J^{\alpha}_{ij} = \frac{\partial\Delta\gamma^{\alpha}}{\partial U_{ij}} \approx \frac{\partial\Delta\gamma^{\alpha}}{\partial S_{mn}}\frac{\partial S_{mn}}{\partial U_{ij}} = M^{\alpha}_{mn}\mathcal{Q}_{mnij}, \tag{51}$$

where $\boldsymbol{M}^{\alpha}$ is also calculated with the approximation:

$$\boldsymbol{M}^{\alpha} = \frac{\partial\Delta\gamma^{\alpha}}{\partial\boldsymbol{S}} = \frac{\partial\Delta\gamma^{\alpha}}{\partial\tau^{\alpha}}\frac{\partial\tau^{\alpha}}{\partial\boldsymbol{S}} \approx \frac{\partial\Delta\gamma^{\alpha}}{\partial\tau^{\alpha}}\mathrm{sym}(\boldsymbol{S}^{\alpha}_{0}), \tag{52}$$

therefore,

$$M^{\alpha}_{ij} = \frac{\partial\Delta\gamma^{\alpha}}{\partial\tau^{\alpha}}\mathrm{sym}(S^{\alpha}_{0,ij}). \tag{53}$$

The elementary derivative $\dfrac{\partial\Delta\gamma^{\alpha}}{\partial\tau^{\alpha}}$ depends on the flow rule adopted. Here, considering the power-law outlined in Eq. (12) and the simplest case where $\tau^{\alpha} > 0$, we have:

$$\frac{\partial\Delta\gamma^{\alpha}}{\partial\tau^{\alpha}} = n\frac{\Delta\gamma^{\alpha}}{\tau^{\alpha}}, \tag{54}$$

finally, substituting Eqs. (41) in (42) and solving for $\mathcal{Q}_{ijkl}$ yields:

$$\mathcal{Q}_{ijkl} = \left[\delta_{im}\delta_{jn} + \sum_{\alpha} C^{\alpha}_{ij}M^{\alpha}_{mn}\right]^{-1}\left[\mathcal{D}_{mnkl} - \sum_{\alpha}\Delta\gamma^{\alpha}\Gamma^{\alpha}_{mnkl}\right]. \tag{55}$$

Algorithm for computing $\mathbb{W}^{\boldsymbol{\sigma},\boldsymbol{E}}$

The analytical calculation of the mechanical Jacobian follows the steps:

- 1. $\Theta_{ij} = \delta_{ij} - \Delta\theta\beta_{ij}$
- 2. $A_{ij} = F^{\mathrm{p}\,-\mathrm{T}}_{im}(t)\Theta_{mn}F^{\theta\,-\mathrm{T}}_{np}(t)U_{pq}U_{qs}F^{\theta\,-1}_{sw}(t)\Theta_{wr}F^{\mathrm{p}\,-1}_{rj}(t)$
- 3. $C^{\alpha}_{ij} = \frac{1}{2}\mathbb{C}_{ijmn}\left(A_{mp}S^{\alpha}_{0,pn} + S^{\alpha\,\mathrm{T}}_{0,mp}A_{pn}\right)$
- 4. $\mathcal{E}_{ijkl} = F^{\mathrm{p}\,-\mathrm{T}}_{im}(t)\Theta_{mn}(t)F^{\theta\,-\mathrm{T}}_{nk}(t)U_{ls}F^{\theta\,-1}_{sw}(t)\Theta_{wr}(t)F^{\mathrm{p}\,-1}_{rj}(t) + F^{\mathrm{p}\,-\mathrm{T}}_{im}(t)\Theta_{mn}(t)F^{\theta\,-\mathrm{T}}_{np}(t)U_{pk}F^{\theta\,-1}_{lw}(t)\Theta_{wr}(t)F^{\mathrm{p}\,-1}_{rj}(t)$
- 5. $\mathcal{D}_{ijkl} = \frac{1}{2}\mathbb{C}_{ijmn}\mathcal{E}_{mnkl}$
- 6. $\Gamma^{\alpha}_{ijkl} = \frac{1}{2}\mathbb{C}_{ijmn}\left(\mathcal{E}_{mpkl}S^{\alpha}_{0,pn} + S^{\alpha\,\mathrm{T}}_{0,mp}\mathcal{E}_{pnkl}\right)$
- 7. $M^{\alpha}_{ij} = \frac{\partial\Delta\gamma^{\alpha}}{\partial\tau^{\alpha}}\mathrm{sym}(S^{\alpha}_{0,ij})$
- 8. $\mathcal{Q}_{ijkl} = \left[\delta_{im}\delta_{jn} + \sum C^{\alpha}_{ij}M^{\alpha}_{mn}\right]^{-1}\left[\mathcal{D}_{mnkl} - \sum\Delta\gamma^{\alpha}\Gamma^{\alpha}_{mnkl}\right]$
- 9. $J^{\alpha}_{ij} = M^{\alpha}_{mn}\mathcal{Q}_{mnij}$
- 10. $K_{ij} = F^{\mathrm{p}}_{im}(t)\Theta_{mn}F^{\mathrm{p}\,-1}_{nj}(t)$
- 11. $\mathcal{T}_{ijkl} = R_{ik}F^{\mathrm{e}}_{lp}(t)K_{pj}(t) - R_{ik}F^{\mathrm{e}}_{lp}(t)K_{pq}(t)\sum\Delta\gamma^{\alpha}S^{\alpha}_{0,qj} - R_{im}U_{mn}F^{\mathrm{e}}_{np}(t)K_{pq}(t)\sum J^{\alpha}_{kl}S^{\alpha}_{0,qj}$
- 12. $\mathbb{W}^{\boldsymbol{\sigma},\boldsymbol{E}}_{ijkl} = \frac{1}{\det\boldsymbol{F}^{\mathrm{e}}}\left[\mathcal{T}_{imkl}S_{mn}F^{\mathrm{e}\mathrm{T}}_{nj} + F^{\mathrm{e}}_{im}\mathcal{Q}_{mnkl}F^{\mathrm{e}\mathrm{T}}_{nj} + F^{\mathrm{e}}_{im}S_{mn}\mathcal{T}_{jnkl} - F^{\mathrm{e}}_{im}S_{mn}F^{\mathrm{e}\mathrm{T}}_{nj}\mathcal{T}_{pqkl}F^{\mathrm{e}\,-1}_{qp}\right]$

Thermomechanical Jacobian: $\mathbb{W}^{\boldsymbol{\sigma},\boldsymbol{\theta}}$

The first thermomechanical Jacobian used in the implicit backward Euler integration scheme is defined as:

$$\mathbb{W}^{\boldsymbol{\sigma},\theta} = \frac{\partial\boldsymbol{\sigma}}{\partial\theta}. \tag{56}$$

Recalling Eq. (10) for the CAUCHY stress tensor, we have:

$$\mathbb{W}^{\boldsymbol{\sigma},\theta}_{ij} = \frac{1}{\det\boldsymbol{F}^{\mathrm{e}}}F^{\mathrm{e}}_{im}\frac{\partial S_{mn}}{\partial\theta}F^{\mathrm{e}\mathrm{T}}_{nj}. \tag{57}$$

The definition of the second PIOLA- KIRCHHOFF stress tensor, yields:

$$\boldsymbol{S} = \mathbb{C} : \boldsymbol{E}^{e} \Rightarrow \frac{\partial S_{ij}}{\partial\theta} = \frac{\partial\mathbb{C}_{ijkl}}{\partial\theta}E^{e}_{kl}. \tag{58}$$

The temperature dependence of the elasticity tensor in the global basis can be assessed with Eqs. (8) and (9):

$$\begin{aligned}\mathbb{C}_{ijkl} = \tilde{R}_{im}\tilde{R}_{jn}\tilde{R}_{kp}\tilde{R}_{lq}\mathbb{C}^{c}_{mnpq} &= \tilde{R}_{im}\tilde{R}_{jn}\tilde{R}_{kp}\tilde{R}_{lq}\mathbb{C}^{0}_{mnpq}\\ &+ \tilde{R}_{im}\tilde{R}_{jn}\tilde{R}_{kp}\tilde{R}_{lq}\mathbb{M}_{mnpq}\theta,\end{aligned} \tag{59}$$

hence,

$$\frac{\partial\mathbb{C}_{ijkl}}{\partial\theta} = \tilde{R}_{im}\tilde{R}_{jn}\tilde{R}_{kp}\tilde{R}_{lq}\mathbb{M}_{mnpq}$$

$$\Rightarrow \frac{\partial S_{ij}}{\partial \theta} = \tilde{R}_{im}\tilde{R}_{jn}\tilde{R}_{kp}\tilde{R}_{lq}\mathbb{M}_{mnpq}E^{e}_{kl}, \tag{60}$$

and finally:

$$\mathbb{W}^{\boldsymbol{\sigma},\theta}_{ij} = \frac{1}{\det \boldsymbol{F}^{\mathrm{e}}} F^{\mathrm{e}}_{im}\tilde{R}_{mp}\tilde{R}_{nq}\tilde{R}_{ks}\tilde{R}_{lr}\mathbb{M}_{pqsr}E^{e}_{kl}F^{\mathrm{e}\,\mathrm{T}}_{nj}. \tag{61}$$

Algorithm for computing $\mathbb{W}^{\boldsymbol{\sigma},\boldsymbol{\theta}}$

The analytical calculation of the first thermomechanical Jacobian follows the steps:

- 1. $\frac{\partial S_{mn}}{\partial \theta} = \tilde{R}_{mp}\tilde{R}_{nq}\tilde{R}_{ks}\tilde{R}_{lr}\mathbb{M}_{pqsr}E^{e}_{kl}$
- 2. $\mathbb{W}^{\boldsymbol{\sigma},\theta}_{ij} = \frac{1}{\det \boldsymbol{F}^{\mathrm{e}}} F^{\mathrm{e}}_{im}\frac{\partial S_{mn}}{\partial \theta}F^{\mathrm{e}\,\mathrm{T}}_{nj}$

9.1 Thermomechanical Jacobian: $\mathbb{W}^{\dot{\boldsymbol{Q}},\boldsymbol{E}}$

The second thermomechanical Jacobian used in the implicit backward Euler integration scheme is defined as:

$$\mathbb{W}^{\dot{Q},\boldsymbol{E}} = \frac{\partial \dot{Q}}{\partial \boldsymbol{E}_t}. \tag{62}$$

We initially start with the approximation outlined in Eq. (31), precisely:

$$\partial \boldsymbol{E}_t \approx \partial \boldsymbol{U}_t \Rightarrow \mathbb{W}^{\dot{Q},\boldsymbol{E}} \approx \frac{\partial \dot{Q}}{\partial \boldsymbol{U}_t}. \tag{63}$$

From Eq. (19) we have:

$$\dot{Q} = \eta \sum_{\alpha=1}^{n} \tau^{\alpha}\dot{\gamma}^{\alpha}, \tag{64}$$

hence,

$$\mathbb{W}^{\dot{Q},\boldsymbol{E}}_{ij} = \eta \sum_{\alpha=1}^{n} \left(H^{\alpha}_{ij}\Delta\gamma^{\alpha} + \tau^{\alpha}J^{\alpha}_{ij} \right), \tag{65}$$

where,

$$H^{\alpha}_{ij} = \frac{\partial \tau^{\alpha}}{\partial U_{ij}} \quad \text{and} \quad J^{\alpha}_{ij} = \frac{\partial \Delta\gamma^{\alpha}}{\partial U_{ij}}. \tag{66}$$

We recall that J^{α}_{ij} has been computed in Sect. 1 and proceed with the calculation of H^{α}_{ij} only. Substituting Eqs. (11) in (66) yields:

$$H^{\alpha}_{ij} = \frac{\partial \tau^{\alpha}}{\partial U_{ij}} \Rightarrow H^{\alpha}_{ij} = \det \boldsymbol{F}^{\theta}\left(F^{\theta\,\mathrm{T}}_{km}\frac{\partial S_{mn}}{\partial U_{ij}}F^{\theta\,-\mathrm{T}}_{nl}S^{\alpha}_{0,kl} \right), \tag{67}$$

noting that $\mathcal{Q}_{ijkl} = \frac{\partial S_{ij}}{\partial U_{kl}}$ has been computed in Sect. 1, we finally have:

$$H^{\alpha}_{ij} = \det \boldsymbol{F}^{\theta}\left(F^{\theta\,\mathrm{T}}_{km}\mathcal{Q}_{mnij}F^{\theta\,-\mathrm{T}}_{nl}S^{\alpha}_{0,kl} \right). \tag{68}$$

9.1.1 Algorithm for computing $\mathbb{W}^{\dot{\boldsymbol{Q}},\boldsymbol{E}}$

The analytical calculation of the second thermomechanical Jacobian, assuming items 1 through 9 in Sect. 9.0.7 have been computed, follows the steps:

- 1. $H^{\alpha}_{ij} = \det \boldsymbol{F}^{\theta}\left(F^{\theta\,\mathrm{T}}_{km}\mathcal{Q}_{mnij}F^{\theta\,-\mathrm{T}}_{nl}S^{\alpha}_{0,kl} \right)$
- 2. $\mathbb{W}^{\dot{Q},\boldsymbol{E}}_{ij} = \eta \sum_{\alpha} \left(H^{\alpha}_{ij}\Delta\gamma^{\alpha} + \tau^{\alpha}J^{\alpha}_{ij} \right)$

9.2 Thermal Jacobian: $\mathbb{W}^{\dot{\boldsymbol{Q}},\boldsymbol{\theta}}$

The thermal Jacobian used in the implicit backward Euler integration scheme is defined as:

$$\mathbb{W}^{\dot{Q},\theta} = \frac{\partial \dot{Q}}{\partial \theta}. \tag{69}$$

From Eq. (19) we have:

$$\mathbb{W}^{\dot{Q},\theta} = \frac{\partial \dot{Q}}{\partial \theta} = \eta \sum_{\alpha} \left(\frac{\partial \tau^{\alpha}}{\partial \theta}\Delta\gamma^{\alpha} + \tau^{\alpha}\frac{\partial \Delta\gamma^{\alpha}}{\partial \theta} \right). \tag{70}$$

Before proceeding with the calculation of the first derivative in Eq. (70), we recall the following results:

$$\frac{\partial \boldsymbol{F}^{\theta}}{\partial \theta} = \boldsymbol{F}^{\theta}\boldsymbol{\beta}, \quad \frac{\partial \det \boldsymbol{F}^{\theta}}{\partial \theta} = \det \boldsymbol{F}^{\theta}\,\mathrm{Tr}\,\boldsymbol{\beta}, \tag{71}$$

where $\boldsymbol{\beta}$ is the diagonal thermal expansion tensor. We proceed with the calculation of the first term, precisely:

$$\frac{\partial \tau^{\alpha}}{\partial \theta} = \frac{\partial}{\partial \theta}\left[\det \boldsymbol{F}^{\theta}\left(\boldsymbol{F}^{\theta\,\mathrm{T}}\boldsymbol{S}\boldsymbol{F}^{\theta\,-\mathrm{T}} \right) : \boldsymbol{S}^{\alpha}_{0} \right], \tag{72}$$

$$\begin{aligned} &= \det \boldsymbol{F}^{\theta}\,\mathrm{Tr}\,\boldsymbol{\beta}\left(\boldsymbol{F}^{\theta\,\mathrm{T}}\boldsymbol{S}\boldsymbol{F}^{\theta\,-\mathrm{T}} \right) : \boldsymbol{S}^{\alpha}_{0} \\ &\quad + \det \boldsymbol{F}^{\theta}\left(\boldsymbol{F}^{\theta}\boldsymbol{\beta}\boldsymbol{S}\boldsymbol{F}^{\theta\,-\mathrm{T}} + \boldsymbol{F}^{\theta\,\mathrm{T}}\frac{\partial \boldsymbol{S}}{\partial \theta}\boldsymbol{F}^{\theta\,-\mathrm{T}} \right. \\ &\quad \left. -\boldsymbol{F}^{\theta\,\mathrm{T}}\boldsymbol{S}\boldsymbol{\beta}\boldsymbol{F}^{\theta\,-\mathrm{T}} \right) : \boldsymbol{S}^{\alpha}_{0}, \end{aligned} \tag{73}$$

$$\approx \det \boldsymbol{F}^{\theta}\left(\boldsymbol{F}^{\theta\,\mathrm{T}}\frac{\partial \boldsymbol{S}}{\partial \theta}\boldsymbol{F}^{\theta\,-\mathrm{T}} \right) : \boldsymbol{S}^{\alpha}_{0}. \tag{74}$$

The approximation above is due to the small magnitude of the thermal expansion coefficients composing $\boldsymbol{\beta}$. Additionally, the expression for $\frac{\partial \boldsymbol{S}}{\partial \theta}$ has been calculated in Eq. (60). In index form we have:

$$\frac{\partial \tau^\alpha}{\partial \theta} = \det \boldsymbol{F}^\theta \left(F_{ij}^{\theta\,\mathrm{T}} \frac{\partial S_{jk}}{\partial \theta} F_{kl}^{\theta\,-\mathrm{T}} S_{0,il}^\alpha \right), \tag{75}$$

The second derivative in Eq. (70) is obtained straightforwardly through the chain rule:

$$\frac{\partial \Delta\gamma^\alpha}{\partial \theta} = \frac{\partial \Delta\gamma^\alpha}{\partial \tau^\alpha} \frac{\partial \tau^\alpha}{\partial \theta}, \tag{76}$$

where $\frac{\partial \Delta\gamma^\alpha}{\partial \tau^\alpha}$ has been calculated in Eq. (9.0.7).

9.2.1 Algorithm for computing $\mathbb{W}^{\dot{Q},\theta}$

The analytical calculation of the thermal Jacobian follows, assuming item 1 in Sect. 9.0.7 has been computed, follows the steps:

- 1. $\frac{\partial \tau^\alpha}{\partial \theta} = \det \boldsymbol{F}^\theta \left(F_{ij}^{\theta\,\mathrm{T}} \frac{\partial S_{jk}}{\partial \theta} F_{kl}^{\theta\,-\mathrm{T}} S_{0,il}^\alpha \right)$
- 2. $\frac{\partial \Delta\gamma^\alpha}{\partial \theta} = \frac{\partial \Delta\gamma^\alpha}{\partial \tau^\alpha} \frac{\partial \tau^\alpha}{\partial \theta}$
- 3. $\mathbb{W}^{\dot{Q},\theta} = \frac{\partial \dot{Q}}{\partial \theta} = \eta \sum_\alpha \left(\frac{\partial \tau^\alpha}{\partial \theta} \Delta\gamma^\alpha + \tau^\alpha \frac{\partial \Delta\gamma^\alpha}{\partial \theta} \right)$

10 Appendix B

See Table 2.

Table 2 $\{111\}\langle 110\rangle$ slip systems for FCC crystals following the notation from Schmid and Boas [74]

Slip system	Slip plane normal	Slip direction
A2	$(\bar{1}11)$	$[0\bar{1}1]$
A3	$(\bar{1}11)$	$[101]$
A6	$(\bar{1}11)$	$[110]$
B2	(111)	$[0\bar{1}1]$
B4	(111)	$[\bar{1}01]$
B5	(111)	$[\bar{1}10]$
C1	$(\bar{1}\bar{1}1)$	$[011]$
C3	$(\bar{1}\bar{1}1)$	$[101]$
C5	$(\bar{1}\bar{1}1)$	$[\bar{1}10]$
D1	$(1\bar{1}1)$	$[011]$
D4	$(1\bar{1}1)$	$[\bar{1}01]$
D6	$(1\bar{1}1)$	$[110]$

Acknowledgements Anderson Nascimento and Irene J. Beyerlein are grateful for the support of the National Science Foundation under grant number 2051390. Akhilesh Pedgaonkar and Curt A. Bronkhorst are grateful for the support of the National Science Foundation under grant number 2051355. Use was made of computational facilities purchased with funds from the National Science Foundation (CNS-1725797) and administered by the Center for Scientific Computing (CSC). The CSC is supported by the California NanoSystems Institute and the Materials Research Science and Engineering Center (MRSEC; NSF DMR 2308708) at UC Santa Barbara.

References

1. Agaram S, Kanjarla AK, Bhuvaraghan B, Srinivasan SM (2021) Dislocation density based crystal plasticity model incorporating the effect of precipitates in IN718 under monotonic and cyclic deformation. Int J Plast 141:102990. https://doi.org/10.1016/J.IJPLAS.2021.102990
2. Anand L (2004) Single-crystal elasto-viscoplasticity: application to texture evolution in polycrystalline metals at large strains. Comput Methods Appl Mech Eng 193:5359–5383. https://doi.org/10.1016/J.CMA.2003.12.068
3. Arsenlis A, Parks DM (2002) Modeling the evolution of crystallographic dislocation density in crystal plasticity. J Mech Phys Solids 50:1979–2009
4. Balasubramanian S (1998) Polycrystalline plasticity: application to deformation processing of lightweight metals. Massachusetts Institute of Technology
5. Bastola N, Jahan MP, Rangasamy N, Rakurty CS (2023) A review of the residual stress generation in metal additive manufacturing: analysis of cause, measurement, effects, and prevention. Micromachines 14:1480. https://doi.org/10.3390/MI14071480
6. Bennett KC, Zecevic M, Luscher DJ, Lebensohn RA (2020) A thermo-elastoplastic self-consistent homogenization method for inter-granular plasticity with application to thermal ratcheting of TATB. Adv Model Simul Eng Sci 7:1–32. https://doi.org/10.1186/S40323-019-0139-6
7. Bertsch KM, Meric de Bellefon G, Kuehl B, Thoma DJ (2020) Origin of dislocation structures in an additively manufactured austenitic stainless steel 316L. Acta Mater 199:19–33. https://doi.org/10.1016/J.ACTAMAT.2020.07.063
8. Beyerlein IJ, Tomé CN (2008) A dislocation-based constitutive law for pure Zr including temperature effects. Int J Plast 24:867–895. https://doi.org/10.1016/J.IJPLAS.2007.07.017
9. Bhattacharyya JJ, Pagan DC, Agnew SR (2021) Large rotations of the grain-scale stress tensor during yielding set the stage for failure. Int J Plast 146:103087. https://doi.org/10.1016/J.IJPLAS.2021.103087
10. Bronkhorst CA, Mayeur JR, Livescu V, Pokharel R, Brown DW, Gray GT (2019) Structural representation of additively manufactured 316L austenitic stainless steel. Int J Plast 118:70–86. https://doi.org/10.1016/J.IJPLAS.2019.01.012
11. Chan KS (2023) Incorporating dislocation mechanisms into a phenomenological cyclic plasticity model for structural alloys. Metall Mater Trans A Phys Metall Mater Sci 54:3431–3447. https://doi.org/10.1007/S11661-023-07107-8
12. Charpagne MA, Hestroffer JM, Polonsky AT, Echlin MP, Texier D, Valle V, Beyerlein IJ, Pollock TM, Stinville JC (2021) Slip localization in Inconel 718: a three-dimensional and statistical perspective. Acta Materialia 215:117037. https://doi.org/10.1016/J.ACTAMAT.2021.117037
13. Chen W, Voisin T, Zhang Y, Florien JB, Spadaccini CM, McDowell DL, Zhu T, Wang YM (2019) Microscale residual stresses in addi-

tively manufactured stainless steel. Nat Commun 10:1–12. https://doi.org/10.1038/s41467-019-12265-8

14. Clayton JD (2005) Dynamic plasticity and fracture in high density polycrystals: constitutive modeling and numerical simulation. J Mech Phys Solids 53:261–301. https://doi.org/10.1016/J.JMPS.2004.06.009
15. Cocke CK, Rollett AD, Lebensohn RA, Spear AD (2021) The AFRL additive manufacturing modeling challenge: predicting micromechanical fields in AM IN625 using an FFT-based method with direct input from a 3D microstructural image. Integr Mater Manuf Innov 10:157–176. https://doi.org/10.1007/S40192-021-00211-W
16. Connolly DS, Kohar CP, Muhammad W, Hector LG, Mishra RK, Inal K (2020) A coupled thermomechanical crystal plasticity model applied to quenched and partitioned steel. Int J Plast 133:102757. https://doi.org/10.1016/J.IJPLAS.2020.102757
17. Dai H (1997) Geometrically-necessary dislocation density in continuum plasticity theory. Massachusetts Institute of Technology
18. Denlinger ER, Irwin J, Michaleris P (2014) Thermomechanical modeling of additive manufacturing large parts. J Manuf Sci Eng Trans ASME 136:061007. https://doi.org/10.1115/1.4028669
19. Diani J, Liu Y, Gall K (2006) Finite strain 3D thermoviscoelastic constitutive model for shape memory polymers. Polym Eng Sci 46:486–492. https://doi.org/10.1002/PEN.20497
20. Diehl M (2017) Review and outlook: mechanical, thermodynamic, and kinetic continuum modeling of metallic materials at the grain scale. MRS Commun 7:735–746. https://doi.org/10.1557/MRC.2017.98
21. Dunne FP, Kiwanuka R, Wilkinson AJ (2012) Crystal plasticity analysis of micro-deformation, lattice rotation and geometrically necessary dislocation density. Proc R Soc A Math Phys Eng Sci 468:2509–2531. https://doi.org/10.1098/RSPA.2012.0050
22. Dye D, Stone HJ, Reed RC (2001) Intergranular and interphase microstresses. Curr Opin Solid State Mater Sci 5:31–37. https://doi.org/10.1016/S1359-0286(00)00019-X
23. Essmann U, Mughrabi H (1979) Annihilation of dislocations during tensile and cyclic deformation and limits of dislocation densities. Philos Mag A 40:731–756. https://doi.org/10.1080/01418617908234871
24. Foley DL, Latypov MI, Zhao X, Hestroffer J, Beyerlein IJ, Lamberson LE, Taheri ML (2022) Geometrically necessary dislocation density evolution as a function of microstructure and strain rate. Mater Sci Eng A 831:142224. https://doi.org/10.1016/J.MSEA.2021.142224
25. Forni D, Mazzucato F, Valente A, Cadoni E (2021) High strain-rate behaviour of as-cast and as-build Inconel 718 alloys at elevated temperatures. Mech Mater 159:061007. https://doi.org/10.1016/J.MECHMAT.2021.103859
26. Franceschi A, Stahl J, Kock C, Selbmann R, Ortmann-Ishkina S, Jobst A, Merklein M, Kuhfuß B, Bergmann M, Behrens BA, Volk W, Groche P (2021) Strategies for residual stress adjustment in bulk metal forming. Arch Appl Mech 91:3557–3577. https://doi.org/10.1007/S00419-021-01903-7
27. Franciosi P, Berveiller M, Zaoui A (1980) Latent hardening in copper and aluminium single crystals. Acta Metallurgica 28:273–283. https://doi.org/10.1016/0001-6160(80)90162-5
28. Francis EM, Grant BM, Fonseca JQD, Phillips PJ, Mills MJ, Daymond MR, Preuss M (2014) High-temperature deformation mechanisms in a polycrystalline nickel-base superalloy studied by neutron diffraction and electron microscopy. Acta Materialia 74:18–29. https://doi.org/10.1016/J.ACTAMAT.2014.04.028
29. Francois MM, Sun A, King WE, Henson NJ, Tourret D, Bronkhorst CA, Carlson NN, Newman CK, Haut T, Bakosi J, Gibbs JW, Livescu V, Vander Wiel SA, Clarke AJ, Schraad MW, Blacker T, Lim H, Rodgers T, Owen S, Abdeljawad F, Madison J, Anderson AT, Fattebert JL, Ferencz RM, Hodge NE, Khairallah SA, Walton O (2017) Modeling of additive manufacturing processes for metals: challenges and opportunities. Curr Opin Solid State Mater Sci 21:198–206. https://doi.org/10.1016/J.COSSMS.2016.12.001
30. Frazier WE (2014) Metal additive manufacturing: a review. J Mater Eng Perform 23:1917–1928. https://doi.org/10.1007/s11665-014-0958-z
31. Ghorbanpour S, Alam ME, Ferreri NC, Kumar A, McWilliams BA, Vogel SC, Bicknell J, Beyerlein IJ, Knezevic M (2020) Experimental characterization and crystal plasticity modeling of anisotropy, tension-compression asymmetry, and texture evolution of additively manufactured Inconel 718 at room and elevated temperatures. Int J Plast 125:63–79. https://doi.org/10.1016/J.IJPLAS.2019.09.002
32. Ghorbanpour S, Deshmukh K, Sahu S, Riemslag T, Reinton E, Borisov E, Popovich A, Bertolo V, Jiang Q, Sanchez MT, Knezevic M, Popovich V (2022) Additive manufacturing of functionally graded inconel 718: effect of heat treatment and building orientation on microstructure and fatigue behaviour. J Mater Process Technol 306:117573. https://doi.org/10.1016/J.JMATPROTEC.2022.117573
33. Ghorbanpour S, Zecevic M, Kumar A, Jahedi M, Bicknell J, Jorgensen L, Beyerlein IJ, Knezevic M (2017) A crystal plasticity model incorporating the effects of precipitates in superalloys: application to tensile, compressive, and cyclic deformation of Inconel 718. Int J Plast 99:162–185. https://doi.org/10.1016/J.IJPLAS.2017.09.006
34. Godec M, Malej S, Feizpour D, Donik, Balažic M, Klobčar D, Pambaguian L, Conradi M, Kocijan A (2021) Hybrid additive manufacturing of Inconel 718 for future space applications. Mater Charact 172:110842. https://doi.org/10.1016/J.MATCHAR.2020.110842
35. Grilli N, Hu D, Yushu D, Chen F, Yan W (2022) Crystal plasticity model of residual stress in additive manufacturing using the element elimination and reactivation method. Comput Mech 69:825–845. https://doi.org/10.1007/S00466-021-02116-Z
36. Hansen BL, Carpenter JS, Sintay SD, Bronkhorst CA, McCabe RJ, Mayeur JR, Mourad HM, Beyerlein IJ, Mara NA, Chen SR, Gray GT (2013) Modeling the texture evolution of Cu/Nb layered composites during rolling. Int J Plast 49:71–84. https://doi.org/10.1016/J.IJPLAS.2013.03.001
37. Hellebrand S, Brands D, Schröder J, Scheunemann L (2022) A multiscale approach to investigate residual stresses due to targeted cooling of hot bulk formed parts. In: Proceedings of the 8th international conference on structural engineering, mechanics and computation, CRC Press. pp 262–268. https://doi.org/10.1201/9781003348443-41
38. Hestroffer JM, Latypov MI, Stinville JC, Charpagne MA, Valle V, Miller MP, Pollock TM, Beyerlein IJ (2022) Development of grain-scale slip activity and lattice rotation fields in Inconel 718. Acta Materialia 226:117627. https://doi.org/10.1016/J.ACTAMAT.2022.117627
39. Hestroffer JM, Stinville JC, Charpagne MA, Miller MP, Pollock TM, Beyerlein IJ (2023) Slip localization behavior at triple junctions in nickel-base superalloys. Acta Materialia 249:118801. https://doi.org/10.1016/J.ACTAMAT.2023.118801
40. Ho CY, Taylor RE (1998) Thermal expansion of solids. ASM International
41. Horstemeyer MF (2012) Integrated computational materials engineering (ICME) for metals: using multiscale modeling to invigorate engineering design with science. John Wiley and Sons. https://doi.org/10.1002/9781118342664
42. Hosseini E, Popovich VA (2019) A review of mechanical properties of additively manufactured Inconel 718. AdditiveManufacturing 30:100877. https://doi.org/10.1016/j.addma.2019.100877
43. Hu D, Grilli N, Wang L, Yang M, Yan W (2022) Microscale residual stresses in additively manufactured stainless steel: computational

simulation. J Mech Phys Solids 161:104822. https://doi.org/10.1016/J.JMPS.2022.104822

44. Hu D, Grilli N, Yan W (2023) Dislocation structures formation induced by thermal stress in additive manufacturing: multiscale crystal plasticity modeling of dislocation transport. J Mech Phys Solids 173:105235. https://doi.org/10.1016/J.JMPS.2023.105235
45. Hunter A, Preston DL (2022) Analytic model of dislocation density evolution in fcc polycrystals accounting for dislocation generation, storage, and dynamic recovery mechanisms. Int J Plast 151:103178. https://doi.org/10.1016/j.ijplas.2021.103178
46. Kalidindi SR, Bronkhorst CA, Anand L (1992) Crystallographic texture evolution in bulk deformation processing of FCC metals. J Mech Phys Solids 40:537–569. https://doi.org/10.1016/0022-5096(92)80003-9
47. Lee S, Cho H, Bronkhorst CA, Pokharel R, Brown DW, Clausen B, Vogel SC, Anghel V, Gray GT, Mayeur JR (2023) Deformation, dislocation evolution and the non-Schmid effect in body-centered-cubic single-and polycrystal tantalum. Int J Plast 163:103529. https://doi.org/10.1016/j.ijplas.2023.103529
48. Li C, Liu ZY, Fang XY, Guo YB (2018) Residual stress in metal additive manufacturing. Proc CIRP 71:348–353. https://doi.org/10.1016/J.PROCIR.2018.05.039
49. Li J, Romero I, Segurado J (2019) Development of a thermo-mechanically coupled crystal plasticity modeling framework: application to polycrystalline homogenization. Int J Plast 119:313–330. https://doi.org/10.1016/J.IJPLAS.2019.04.008
50. Lieou CK, Bronkhorst CA (2021) Thermomechanical conversion in metals: dislocation plasticity model evaluation of the Taylor–Quinney coefficient. Acta Mater 202:170–180. https://doi.org/10.1016/J.ACTAMAT.2020.10.037
51. Lieou CK, Mourad HM, Bronkhorst CA (2019) Strain localization and dynamic recrystallization in polycrystalline metals: thermodynamic theory and simulation framework. Int J Plast 119:171–187. https://doi.org/10.1016/J.IJPLAS.2019.03.005
52. Lima-Chaves GD, Upadhyay MV (2024) Finite element implementation of the thermal field dislocation mechanics model: study of temperature evolution due to dislocation activity. Comput Methods Appl Mech Eng 421:116763. https://doi.org/10.1016/j.cma.2024.116763
53. Lindroos M, Pinomaa T, Antikainen A, Lagerbom J, Reijonen J, Lindroos T, Andersson T, Laukkanen A (2021) Micromechanical modeling approach to single track deformation, phase transformation and residual stress evolution during selective laser melting using crystal plasticity. Addit Manuf 38:101819. https://doi.org/10.1016/J.ADDMA.2020.101819
54. Liu F, Lin X, Yang G, Song M, Chen J, Huang W (2011) Microstructure and residual stress of laser rapid formed Inconel 718 nickel-base superalloy. Opt Laser Technol 43:208–213. https://doi.org/10.1016/J.OPTLASTEC.2010.06.015
55. Luscher DJ, Bronkhorst CA, Alleman CN, Addessio FL (2013) A model for finite-deformation nonlinear thermomechanical response of single crystal copper under shock conditions. J Mech Phys Solids 61:1877–1894. https://doi.org/10.1016/J.JMPS.2013.05.002
56. Ma A, Roters F (2004) A constitutive model for fcc single crystals based on dislocation densities and its application to uniaxial compression of aluminium single crystals. Acta Mater 52:3603–3612. https://doi.org/10.1016/J.ACTAMAT.2004.04.012
57. Martin G, Ochoa N, Saï K, Hervé-Luanco E, Cailletaud G (2014) A multiscale model for the elastoviscoplastic behavior of Directionally Solidified alloys: application to FE structural computations. Int J Solids Struct 51:1175–1187. https://doi.org/10.1016/J.IJSOLSTR.2013.12.013
58. McHugh PE, Asaro RJ, Shih CF (1993) Computational modeling of metal matrix composite materials-I. Isothermal deformation patterns in ideal microstructures. Acta Metallurgica et Materialia 41:1461–1476. https://doi.org/10.1016/0956-7151(93)90255-Q
59. McLouth TD, Witkin DB, Lohser JR, Sitzman SD, Adams PM, Lingley ZR, Bean GE, Yang JM, Zaldivar RJ (2021) Temperature and strain-rate dependence of the elevated temperature ductility of Inconel 718 prepared by selective laser melting. Mater Sci Eng. https://doi.org/10.1016/j.msea.2021.141814
60. Mecking H, Kocks UF (1981) Kinetics of flow and strain-hardening. Acta Metall 29:1865–1875. https://doi.org/10.1016/0001-6160(81)90112-7
61. Meier F, Schwarz C, Werner E (2014) Crystal-plasticity based thermo-mechanical modeling of Al-components in integrated circuits. Comput Mater Sci 94:122–131. https://doi.org/10.1016/J.COMMATSCI.2014.03.020
62. Meissonnier FT, Busso EP, O'Dowd NP (2001) Finite element implementation of a generalised non-local rate-dependent crystallographic formulation for finite strains. Int J Plast 17:601–640. https://doi.org/10.1016/S0749-6419(00)00064-4
63. Mercelis P, Kruth JP (2006) Residual stresses in selective laser sintering and selective laser melting. Rapid Prototyp J. https://doi.org/10.1108/13552540610707013
64. Mianroodi JR, Shanthraj P, Liu C, Vakili S, Roongta S, Siboni NH, Perchikov N, Bai Y, Svendsen B, Roters F, Raabe D, Diehl M (2022) Modeling and simulation of microstructure in metallic systems based on multi-physics approaches. NPJ Comput Mater 8:1–15. https://doi.org/10.1038/s41524-022-00764-0
65. Mills KC (2002) Recommended values of thermophysical properties for selected commercial alloys. Woodhead
66. Nadammal N, Mishurova T, Fritsch T, Serrano-Munoz I, Kromm A, Haberland C, Dolabella Portella P, Bruno G (2021) Critical role of scan strategies on the development of microstructure, texture, and residual stresses during laser powder bed fusion additive manufacturing. Addit Manuf. https://doi.org/10.1016/j.addma.2020.101792
67. Nicholson DW (2008) Finite element analysis: thermomechanics of solids. CRC Press. https://doi.org/10.1201/9781420050974
68. Ozturk D, Shahba A, Ghosh S (2016) Crystal plasticity FE study of the effect of thermo-mechanical loading on fatigue crack nucleation in titanium alloys. Fatigue Fract Eng Mater Struct 39:752–769. https://doi.org/10.1111/ffe.12410
69. Peirce D, Asaro RJ, Needleman A (1983) Material rate dependence and localized deformation in crystalline solids. Acta Metall 31:1951–1976. https://doi.org/10.1016/0001-6160(83)90014-7
70. Pokharel R, Patra A, Brown DW, Clausen B, Vogel SC, Gray GT (2019) An analysis of phase stresses in additively manufactured 304L stainless steel using neutron diffraction measurements and crystal plasticity finite element simulations. Int J Plast 121:201–217. https://doi.org/10.1016/J.IJPLAS.2019.06.005
71. Raabe D, Roters F, Barlat F, Chen LQ (2004) Continuum scale simulation of engineering materials. Wiley. https://doi.org/10.1002/3527603786
72. Ren K, Chew Y, Fuh JY, Zhang YF, Bi GJ (2019) Thermo-mechanical analyses for optimized path planning in laser aided additive manufacturing processes. Mater Des 162:80–93. https://doi.org/10.1016/J.MATDES.2018.11.014
73. Roters F, Eisenlohr P, Hantcherli L, Tjahjanto DD, Bieler TR, Raabe D (2010) Overview of constitutive laws, kinematics, homogenization and multiscale methods in crystal plasticity finite-element modeling: Theory, experiments, applications. Acta Mater 58:1152–1211. https://doi.org/10.1016/J.ACTAMAT.2009.10.058
74. Schmid E, Boas W (1935) Kristallplastizität: Mit Besonderer Berücksichtigung der Metalle. Springer-Verlag, Berlin Heidelberg GmbH, Berlin
75. Shanthraj P, Zikry MA (2011) Dislocation density evolution and interactions in crystalline materials. Acta Mater 59:7695–7702. https://doi.org/10.1016/J.ACTAMAT.2011.08.041

76. Singh UP, Swaminathan S, Phanikumar G (2022) Thermo-mechanical approach to study the residual stress evolution in part-scale component during laser additive manufacturing of alloy 718. Mater Des 222:111048. https://doi.org/10.1016/J.MATDES.2022.111048
77. Srikanth A, Zabaras N (1999) A computational model for the finite element analysis of thermoplasticity coupled with ductile damage at finite strains. Int J Numer Methods Eng 45:1569–1605
78. Stinville JC, Lenthe WC, Miao J, Pollock TM (2016) A combined grain scale elastic-plastic criterion for identification of fatigue crack initiation sites in a twin containing polycrystalline nickel-base superalloy. Acta Mater 103:461–473. https://doi.org/10.1016/J.ACTAMAT.2015.09.050
79. Taylor GI, Quinney H (1934) The latent energy remaining in a metal after cold working. Proc R Soc A Math Phys Eng Sci 143:307–326. https://doi.org/10.1098/RSPA.1934.0004
80. Tekumalla S, Seita M, Zaefferer S (2024) Delineating dislocation structures and residual stresses in additively manufactured alloys. Acta Mater 262:119413. https://doi.org/10.1016/J.ACTAMAT.2023.119413
81. Texier D, Milanese J, Jullien M, Genée J, Passieux JC, Bardel D, Andrieu E, Legros M, Stinville JC (2024) Strain localization in the alloy 718 Ni-based superalloy: from room temperature to 650°C. Acta Mater 268:119759. https://doi.org/10.1016/J.ACTAMAT.2024.119759
82. Uebing S, Brands D, Scheunemann L, Kock C, Wester H, Behrens BA, Schröder J (2021) Residual stresses in hot bulk formed parts-A phenomenological approach for the austenite-to-martensite phase transformation. Miner Met Mater Ser. https://doi.org/10.1007/978-3-030-75381-8_196
83. Upadhyay MV (2020) On the thermo-mechanical theory of field dislocations in transient heterogeneous temperature fields. J Mech Phys Solids 145:104150. https://doi.org/10.1016/J.JMPS.2020.104150
84. Upadhyay MV, Slama MBH, Gaudez S, Mohanan N, Yedra L, Hallais S, Héripré E, Tanguy A (2021) Non-oxide precipitates in additively manufactured austenitic stainless steel. Sci Rep 2021(11):1–18. https://doi.org/10.1038/s41598-021-89873-2
85. Wang G, Ouyang H, Fan C, Guo Q, Li Z, Yan W, Li Z (2020) The origin of high-density dislocations in additively manufactured metals. Mater Res Lett 8:283–290. https://doi.org/10.1080/21663831.2020.1751739
86. Weisz-Patrault D (2020) Fast simulation of temperature and phase transitions in directed energy deposition additive manufacturing. Addit Manuf 31:100990. https://doi.org/10.1016/J.ADDMA.2019.100990
87. Weisz-Patrault D, Margerit P, Constantinescu A (2022) Residual stresses in thin walled-structures manufactured by directed energy deposition: in-situ measurements, fast thermo-mechanical simulation and buckling. Addit Manuf 56:102903. https://doi.org/10.1016/J.ADDMA.2022.102903
88. Withers PJ, Bhadeshia HKDH (2001) Residual stress part 1-measurement techniques. Mater Sci Technol 17:355–365
89. Xi N, Ni Z, Fang X, Zhou Y, Tang K, Zhang H, Huang K (2023) Role of δ-phase on mechanical behaviors of additive manufactured Inconel 718: detailed microstructure analysis and crystal plasticity modelling. Int J Plast 168:103708. https://doi.org/10.1016/J.IJPLAS.2023.103708
90. Yi Wang W, Li J, Liu W, Liu ZK (2019) Integrated computational materials engineering for advanced materials: a brief review. Comput Mater Sci 158:42–48. https://doi.org/10.1016/J.COMMATSCI.2018.11.001